DEVELOPMENTAL NEUROSCIENCE

Hierarchical deployment of Tbx3 dictates the identity of hypothalamic KNDy neurons to control puberty onset

Xiang Shi[1,2]†, Yanrong Zhuang[3]†, Zhenhua Chen[1,2]†, Mingrui Xu[1,2], Junqi Kuang[2,4], Xue-Lian Sun[1,2], Lisen Gao[1,2], Xia Kuang[1], Huairen Zhang[1], Wei Li[1,2], Samuel Zheng Hao Wong[5], Chuanyu Liu[6,7], Longqi Liu[6,7,8], Danhua Jiang[1,2], Duanqing Pei[9], Yi Lin[3]*, Qing-Feng Wu[1,2,10,11,12]*

The neuroendocrine system consists of a heterogeneous collection of neuropeptidergic neurons in the brain, among which hypothalamic KNDy neurons represent an indispensable cell subtype controlling puberty onset. Although neural progenitors and neuronal precursors along the cell lineage hierarchy adopt a cascade diversification strategy to generate hypothalamic neuronal heterogeneity, the cellular logic operating within the lineage to specify a subtype of neuroendocrine neurons remains unclear. As human genetic studies have recently established a link between TBX3 mutations and delayed puberty onset, we systematically studied Tbx3-derived neuronal lineage and Tbx3-dependent neuronal specification and found that Tbx3 hierarchically established and maintained the identity of KNDy neurons for triggering puberty. Apart from the well-established lineage-dependent fate determination, we uncovered rules of interlineage interaction and intralineage retention operating through neuronal differentiation in the absence of Tbx3. Moreover, we revealed that human TBX3 mutations disturbed the phase separation of encoded proteins and impaired transcriptional regulation of key neuropeptides, providing a pathological mechanism underlying TBX3-associated puberty disorders.

INTRODUCTION

Puberty is the time in development when the hypothalamic-pituitary-gonadal (HPG) axis is activated to trigger gonadal maturation. Hypothalamic KNDy neurons, residing in arcuate nucleus and coexpressing *Tac2* and *Kiss1*, serve as the nodal regulatory center of puberty onset by controlling gonadotropin-releasing hormone (GnRH) release into the pituitary portal vasculature (*1*, *2*). Within these neurons, neurokinin B encoded by *Tac2* stimulates kisspeptin (encoded by *Kiss1*) release via an autosynaptic routine and substantially contributes to GnRH pulse generation (*1*, *3*, *4*). Although extrinsic factors such as macronutrients and peripheral hormones have been reported to reset the timing of puberty onset by altering the neuropeptide expression or neuronal activity of KNDy neurons (*4*–*6*), the intrinsic factors dictating their identity remain unclear.

Previous human genetic studies focusing on puberty disorders have provided important insights into the intrinsic factors associated with neuronal migration, neuropeptide expression, and activity regulation (*7*, *8*). For instance, among the hitherto identified four monogenic causes of central precocious puberty, three virulence genes (*MKRN3*, *KISS1*, and *KISS1R*) have been suggested to regulate kisspeptin expression and signaling (*9*–*12*). In marked contrast to precocious puberty, idiopathic hypogonadotropic hypogonadism (IHH) with anosmia (defined as Kallmann syndrome) is characterized by delayed or absent puberty, and frequently caused by the defective migration of GnRH neurons into the hypothalamus from nasal placode (*8*, *13*). Loss-of-function mutations in *TBX3* have recently been reported to cause congenital IHH with normal sense of smell (*14*), hinting at its potential roles in processes involved in puberty onset such as the specification of KNDy neuronal identity and regulation of GnRH neuronal migration, although whether and how this occurs remains unknown.

Distinct transcription factor families have been shown to differentially control the fate establishment and identity maintenance of neurons during their differentiation from neural progenitors (*15*, *16*). As a member of T-box family of transcriptional regulators, Tbx3 plays multiple roles in maintaining the pluripotency of embryonic stem cells (ESCs) and induced pluripotent stem cells, regulating mammary gland, limb, and heart development, and contributing to tumor progression (*17*). Tbx3 protein contains a T-box domain required for DNA binding and transcriptional initiation, two repression domains, and an activation domain (*18*). In humans, *TBX3* mutations have been linked to ulnar-mammary syndrome (UMS), an autosomal dominant disease with variable penetrance featured by shortened forelimbs, mammary and apocrine gland hypoplasia, and genital anomalies (*19*). Although patients with *TBX3* mutations have long been found to display a consistent feature of delayed puberty (*20*), *TBX3* has not been regarded as a candidate gene for normosmic IHH until recently (*14*), raising the possibility that it is directly involved in the pathogenesis of delayed puberty onset in UMS patients.

It has recently been suggested that loss of Tbx3 in melanocortin neurons causes metabolic disorders in mice (*21*). To systematically investigate how *Tbx3* mutations cause deficiency in endocrine and metabolic functions, we first traced the cell lineage of Tbx3$^+$ neural

[1]State Key Laboratory of Molecular Development Biology, Institute of Genetics and Developmental Biology, Chinese Academy of Sciences, Beijing 100101, China. [2]University of Chinese Academy of Sciences, Beijing 100101, China. [3]IDG/McGovern Institute for Brain Research, Tsinghua–Peking Joint Centre for Life Sciences, School of Life Sciences, Tsinghua University, Beijing, China. [4]CAS Key Laboratory of Regenerative Biology, Guangzhou Institutes of Biomedicine and Health, Chinese Academy of Sciences, Guangzhou 510530, China. [5]Department of Neurosurgery, Stanford University School of Medicine, Stanford, CA 94305, USA. [6]BGI-ShenZhen, Shenzhen 518103, China. [7]Shenzhen Bay Laboratory, Shenzhen 518000, China. [8]BGI College and Henan Institute of Medical and Pharmaceutical Sciences, Zhengzhou University, Zhengzhou 450000, China. [9]Laboratory of Cell Fate Control, School of Life Sciences, Westlake University, Hangzhou 310024, China. [10]Center for Excellence in Brain Science and Intelligence Technology, Chinese Academy of Sciences, Beijing 100101, China. [11]Chinese Institute for Brain Research, Beijing 102206, China. [12]Beijing Children's Hospital, Capital Medical University, Beijing 100045, China.
*Corresponding author. Email: wu_qingfeng@genetics.ac.cn (Q.-F.W.); linyi@mail.tsinghua.edu.cn (Y.L.)
†These authors contributed equally to this work.

progenitors and mapped the transcriptomic profile of their descendant neurons. Genetic deletion of *Tbx3* at progenitor and neuronal levels disrupted the fate establishment of multiple neuronal subtypes and identity maintenance of a specific neuronal subtype, respectively. Further analysis revealed that phase separation of Tbx3 directed the fate specification of KNDy neurons by transcriptional regulation of their peptidergic identity, thereby precisely controlling the timing of puberty onset. These results provide a systematic view of how *Tbx3* specifies neuronal fate in lineage-dependent and lineage-independent manners, and shed light on the molecular and cellular mechanisms of abnormal sexual maturation in UMS patients.

RESULTS

ATD defined by Tbx3 populates multiple nuclei

In both prenatal and postnatal mouse brains, previous studies have suggested that Tbx3 is specifically expressed in the hypothalamus (*22*, *23*), which has traditionally been subdivided into peduncular and terminal regions along the longitudinal axis. To gain insights into the role of Tbx3 in regulating hypothalamus development and function, we first mapped its expression pattern in prenatal mouse brain and confirmed the specific expression of Tbx3 at the bottom of terminal hypothalamus (Fig. 1A and fig. S1A). It is notable that the Tbx3-defined acroterminal hypothalamic domain supports the updated prosomeric model underlying hypothalamic organization (*24*, *25*). Second, single-cell transcriptomic analysis of two recently published resources mapping the development of mouse hypothalamus showed the expression of *Tbx3* in a subset of neural progenitors and neurons (fig. S1B) (*26*, *27*), which was further corroborated by immunostaining (fig. S1, C to F). Last, we generated a *Tbx3-CreER^{T2}* mouse line in which a tamoxifen-inducible Cre recombinase was inserted into the endogenous *Tbx3* locus using CRISPR-Cas9 (Fig. 1B and fig. S1G), and used *Tbx3-CreER^{T2}::Ai9* mice to validate its genetic labeling of acroterminal progenitor domain (ATD) by tamoxifen induction at embryonic day 9 or 10 (E9 or E10; Fig. 1C and fig. S1, H and I). These results support that Tbx3 defines a specific progenitor domain at the onset of hypothalamus development.

Along the sagittal axis, the hypothalamus is segregated into preoptic, anterior, tuberal, and mammillary zones (*26*). To reveal the spatial specification of Tbx3$^+$ progenitors in diverse hypothalamic nuclei, we genetically labeled ATD with *Tbx3-CreER^{T2}::Ai9* mice and collected the brains at E14, postnatal day 14 (P14), and P21 for analysis. Three-dimensional reconstruction of these brains showed that Tbx3-derived progeny cells were largely restricted within tuberal and mammillary nuclear complex, as compared with the distribution of Rax-derived progeny cells throughout the whole hypothalamus (Fig. 1D, fig. S1J, and movies S1 to S3). Spatial distribution analysis of P14 brains indicated that Tbx3-derived cells populated multiple hypothalamic nuclei including arcuate nucleus (ARC), tuberal nucleus, dorsomedial nucleus, subthalamic nucleus, ventromedial nucleus, posterior hypothalamus, premammillary nucleus, and medial mammillary nucleus (fig. S1K). We next applied a single dose of tamoxifen to *Tbx3-CreER^{T2}::Ai9* mice at three different time points (E9, E11, and E13) for quantitative analyses and found that cells arising from Tbx3$^+$ progenitors exhibited comparatively higher colonization of ARC when induced at later time points (Fig. 1, E to G; fig. S1L; and table S1), implicating a "broad-to-restricted" pattern of Tbx3 expression along the developmental time course (Fig. 1H).

Tbx3$^+$ progenitors generate multiple neuronal subtypes in the hypothalamus

To further elucidate the fate specification of Tbx3-expressing progenitors, we induced genetic labeling by multiple doses of tamoxifen between E9 and E13, and then collected live tdTomato$^+$ progeny cells by fluorescence-activated cell sorting (FACS) at P14 for single-cell RNA sequencing (scRNA-seq) (Fig. 1I). Our unsupervised analysis of 9224 qualified cells clearly discriminated seven principal cell types: neurons (NEU, *Tubb3$^+$Stmn2$^+$*), tanycytes (TC, *Rax$^+$Crym$^+$*), astrocytes (AS, *Slc1a3$^+$Aqp4$^+$Fgfr3$^+$*), oligodendrocyte precursor cells (OPC, *Pdgfra$^+$Sox10$^+$*), pituitary endocrine cells (PEC, *Scg2$^+$Pitx1$^+$*), microglia (MG, *Cx3cr1$^+$Aif1$^+$*), and endothelial cells (EC, *Cldn5$^+$-Ctla2a$^+$Esam$^+$*) (fig. S2, A and B, and table S2). Cell subclustering identified five subgroups of GABAergic (γ-aminobutyric acidergic) neurons and four subtypes of glutamatergic neurons, among which n2 (*Agrp$^+$Sst$^+$*), n4 (*Crabp1$^+$*), n5 (*Tac2$^+$*, i.e., KNDy), n7 (*Pomc$^+$*), and n8 (*Ghrh$^+$*) subclusters resided in ARC (Fig. 1, J and K; fig. S2, C to F; and table S2). We also validated that early Tbx3$^+$ progenitors gave rise to diverse subpopulations of peptidergic neurons in the hypothalamus by single-molecule fluorescence in situ hybridization (smFISH), but only three subtypes of these neurons (*Tac2$^+$* n5, *Agrp$^+$* n2, and *Pomc$^+$* n7), as well as two subclusters of nonpeptidergic neurons (n1 and n4), persisted to express Tbx3 at postnatal stage (Fig. 1, L and M, and fig. S2E). These data collectively suggest that Tbx3-derived progeny cells populate multiple hypothalamic nuclei and diversify into multiple neuronal subtypes, among which the expression of Tbx3 becomes restricted to select subtypes as development proceeds.

Early ablation of *Tbx3* disrupts fate specification of multiple neuronal subtypes

To systematically assess the function of Tbx3 in fate determination of hypothalamic neurons, we generated *Nkx2.1-Cre::Tbx3$^{Flox/Flox}$* (hereafter referred to as NKO) mice to achieve early efficient deletion of *Tbx3* (fig. S3, A to C), and microdissected tuberal and mammillary zones of the P14 hypothalamus for scRNA-seq using the 10× Genomics platform. Notably, we observed that NKO mice were born with a fivefold lower frequency than expected from a normal Mendelian ratio, and NKO pups that survived stereotypically displayed retarded growth (Fig. 2A). After collecting scRNA-seq data from both control and NKO mice, we obtained a total of 45,406 qualified cells for cell typing and further transcriptomic analysis (Fig. 2, B and C; fig. S3D; and table S3). Unsupervised clustering analysis of 1069 neurons subdivided them into 18 subtypes, wherein x3, x12, x13, x14, x16, and x18 subgroups were lost and x15 cluster was gained in the hypothalamus of NKO mice (Fig. 2, C to E, and fig. S3E). After annotating the identity of each neuronal cluster, we found that Tbx3 was at least required for the fate specification of arcuate melanocortin (x3 and x12) and KNDy (x13) neurons, as well as mammillary Hdc (x16) and Foxb1 (x14) neurons (Fig. 2F; fig. S3, F and G; and table S3). Moreover, subclustering analysis of tanycytes, a population of specialized ependymal cells lining the third ventricle, showed that loss of Tbx3 impaired the generation of tanycytes, especially β1 and β2 subtypes residing in the hypothalamic median eminence (fig. S3, H to M).

Given the limited number of collected neurons from scRNA-seq, we further performed single-nucleus RNA-seq (snRNA-seq) of the same tissues using a DNB (DNA nanoballs) platform and harvested 50,872 qualified neurons subsetted from a total of 77,284 cells to reinforce our findings (Fig. 2G and fig. S4A). To taxonomize the

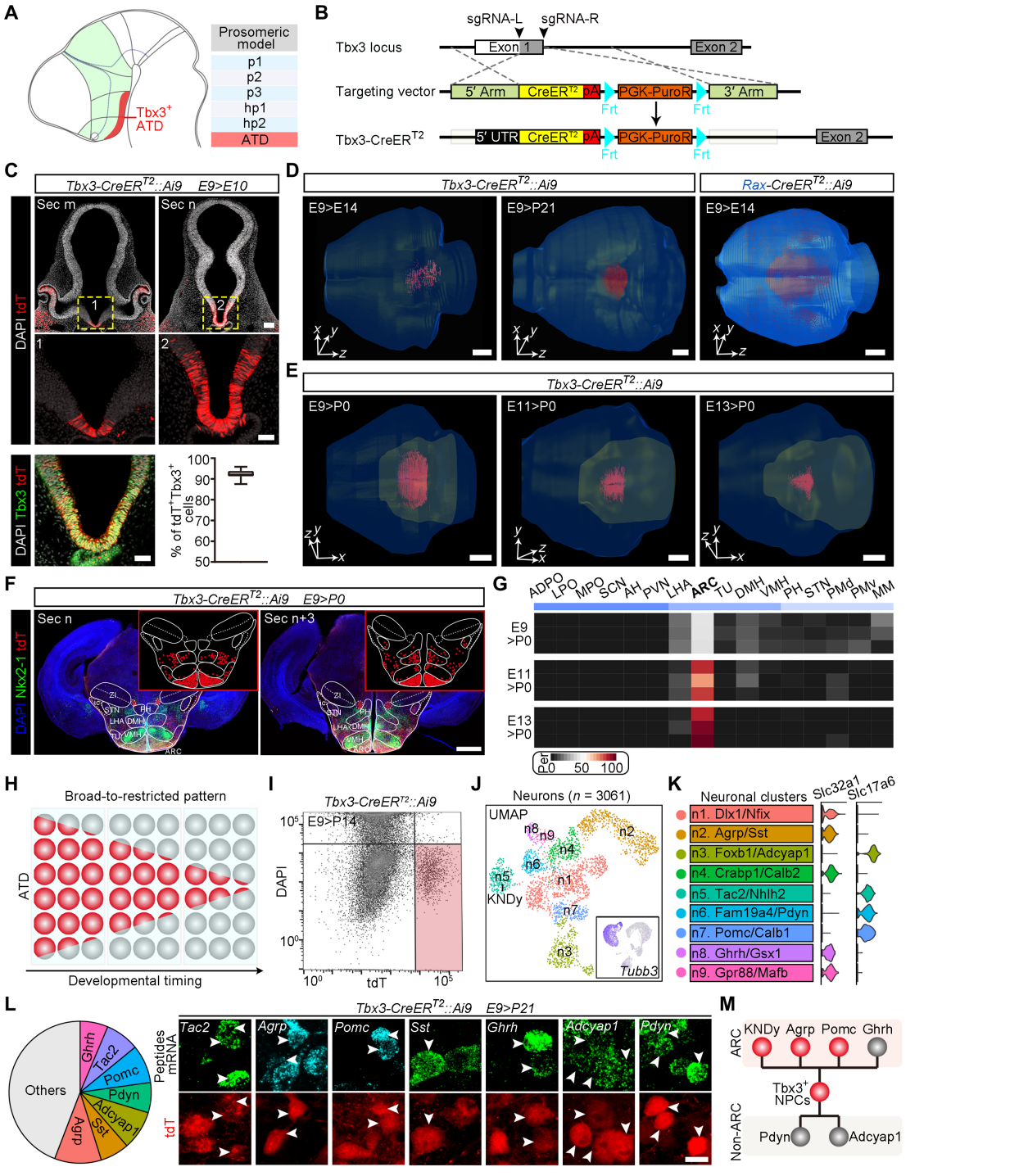

Fig. 1. Tbx3 defines an ATD generating multiple neuronal subtypes. (**A**) Updated prosomeric model supported by the specific expression of Tbx3 in the hypothalamic ATD. (**B**) Targeting strategy for generating *Tbx3-CreER*^{T2} knock-in mouse line. (**C**) Genetic labeling of Tbx3$^+$ neural progenitor cells (NPCs) with *Tbx3-CreER*^{T2}*::Ai9* mice. Quantification shows a high labeling efficiency (~92%) of Tbx3$^+$ progenitors by tdTomato (tdT) at 1 day after tamoxifen induction. Scale bars, 100 and 50 μm. (**D**) Three-dimensional reconstruction of genetically labeled cells in *Tbx3-CreER*^{T2}*::Ai9* and *Rax-CreER*^{T2}*::Ai9* mice. Scale bars, 400, 1000, and 400 μm. (**E**) Three-dimensional reconstruction of fluorescently labeled brains from *Tbx3-CreER*^{T2}*::Ai9* mice. The animals were induced with tamoxifen at E9, E11, or E13 and sacrificed at P0. Scale bars, 700 μm. (**F**) Immunostaining shows the spatial distribution of tdT$^+$ cells arising from Tbx3$^+$ progenitors in P0 hypothalamus. Scale bars, 500 μm. (**G**) Heatmap showing the average percentage of Tbx3-derived tdT$^+$ cells distributed in each hypothalamic nucleus ($n = 3$). (**H**) Schematic diagram showing the broad-to-restricted expression pattern of Tbx3 in ATD. (**I**) Sorting of tdT$^+$ cells from P14 *Tbx3-CreER*^{T2}*::Ai9* brains for scRNA-seq. (**J**) UMAP visualization of 3061 hypothalamic neurons derived from Tbx3$^+$ progenitors. (**K**) Annotation and characterization of neuronal subtypes. Violin plots showing the expression of *Slc32a1* and *Slc17a6* in each cluster. (**L**) Characterization of neuropeptide expression in Tbx3-derived neurons by smFISH. Scale bars, 10 μm. (**M**) Schematic summarizing the derivation of arcuate and nonarcuate peptidergic neurons from Tbx3$^+$ NPCs. KNDy, Agrp, and Pomc neurons persisting to express Tbx3 are highlighted in red.

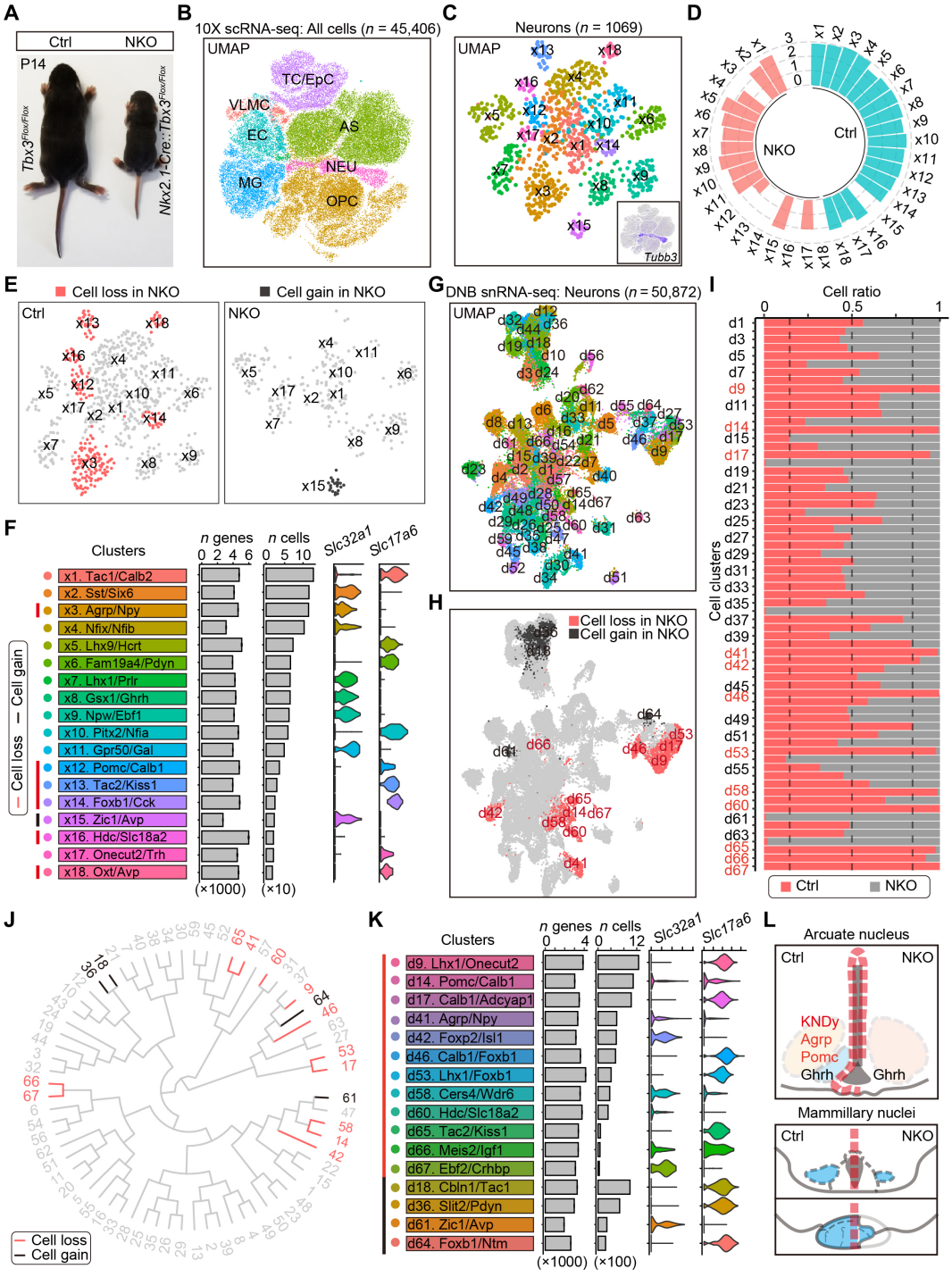

Fig. 2. *Tbx3* deletion at progenitor level disrupts the identity establishment of multiple neuronal subtypes. (**A**) Size comparison of control (Ctrl) and NKO mice at P14 showing the severe growth retardation of Tbx3-deficient mice. (**B**) UMAP visualization of single-cell transcriptomic dataset containing 45,406 hypothalamic cells from P14 control and NKO mice. EpC, ependymal cells; VLMC, vascular leptomeningeal cells. (**C**) Subclustering of 1069 hypothalamic neurons from (B). (**D**) Circular bar chart depicting the normalized proportions of different neuronal subtypes in control and NKO groups. (**E**) UMAP plots showing the loss and gain of neuronal subtypes in NKO hypothalamus. (**F**) Characterization and annotation of 18 neuronal subtypes identified by 10× Genomics platform. Red lines highlight the lost subtypes, and black line indicates the potentially gained cluster (same below). (**G**) UMAP visualization of single-nucleus transcriptomic dataset containing 50,872 hypothalamic neurons. (**H**) UMAP plots showing the loss and gain of neuronal subtypes in NKO hypothalamus. (**I**) Stacked bar plot showing the relative cell ratio of control and NKO groups in each of neuronal subtypes. The three dashed lines represent 20, 50, and 80% of cells, respectively. The neuronal subtypes with a substantial loss in NKO mice are highlighted in red. (**J**) Phylogenetic tree diagram showing the relatedness of neuronal clusters, wherein lost cell clusters are highlighted in red and gained cell clusters are marked in black. (**K**) Characterization and annotation of 12 lost and 4 gained neuronal clusters. (**L**) Schematic diagram summarizing the cell loss in arcuate nucleus and mammillary nuclei within mediobasal hypothalamus of NKO mice.

neuronal clusters within the integrated dataset, we first subdivided them into two major neuronal classes with different neurotransmitters and then cataloged 67 neuronal subtypes with an unsupervised clustering approach (Fig. 2G; fig. S4, B to E; and table S4). Pairwise comparison between control and NKO groups demonstrated a loss of at least 12 neuronal subtypes and a gain of 4 clusters in the Tbx3-deficient hypothalamus (Fig. 2, H to J). The significance of this compositional shift in these neuronal clusters was validated by a combination of three bioinformatics tools including scCODA, Cacoa, and speckle (fig. S4, F and G). We next defined the identity of lost neuronal subtypes and corroborated the finding that Tbx3 specified the arcuate melanocortin (d14 and d41) and KNDy neurons (d65), as well as multiple mammillary neuronal subtypes (d9, d17, d42, d46, d53, and d60) (Fig. 2K and fig. S4H). Pearson correlation analyses of snRNA-seq and scRNA-seq dataset revealed the robust similarity of lost neuronal subtypes in their transcriptomic profiles other than two clusters (d66 and d67) with a small number of cells (fig. S4, I and J). Together, these results compellingly demonstrate the critical function of Tbx3 in specifying multiple neuronal subtypes in both arcuate and mammillary nuclei (Fig. 2L), extending previous findings showing that fate specification of melanocortin neurons depends on Tbx3 (*21*).

Early Tbx3 loss perturbs neuronal fate in lineage-dependent and lineage-independent manners

Our single-cell transcriptomic analysis systematically uncovered the lost and gained neuronal subtypes in Tbx3-deficient brains. To assess whether early deletion of *Tbx3* disrupts neuronal fate in a lineage-dependent manner, we compared the transcriptomic profiles of lost and gained cell subtypes with that of neurons derived from $Tbx3^{+}$ neural progenitors for cell type alignment. Among the lost neuronal subtypes, we found that the absence of KNDy (x13/d65/n5), Agrp (x3/d41/n2), Pomc (x12/d14/n7), and Foxb1 (x14/d9/d17/d46/d53/n3) neurons in *Tbx3*-mutant brains depended on Tbx3 lineage, whereas the depletion of Hdc neurons (x16/d60) occurred in Tbx3 lineage–independent mechanism (Figs. 1, K and M, and 3, A and B). The loss of Agrp, Pomc, and Hdc neurons was experimentally validated in the NKO hypothalamus (Figs. 3, C and D, and 5, A and B). Given that Hdc neurons were not derived from Tbx3 lineage (Fig. 1K and fig. S5C), we speculate that the developmental defect in one neuronal lineage could alter the fate of another cell lineage, suggestive of interlineage interaction. Among the potentially gained neuronal clusters, one cluster (d64) transcriptomically resembled n3 subtype that arose from Tbx3 lineage, while the other clusters (e.g., d18 and d36) might ectopically emerge in the NKO hypothalamus to undergo fate transformation and compensate for cell loss (Fig. 3, A and B, and fig. S5, D to J). Given the border shift of tuberal zone in NKO mice, x15/d61 cluster expressing *Vipr2* might be captured as a microdissection artifact. We found that Ghrh (x8/d59) neurons maintaining growth hormone release were retained in Tbx3-deficient brains (Fig. 2, F and I). Given that Ghrh neurons arose from Tbx3 lineage (Fig. 1M), our data support intralineage retention of specific neuronal subtype in the absence of Tbx3, possibly caused by the unsustainable expression of fate-determining factor. Hence, we show that both cell loss and gain caused by early *Tbx3* deletion could occur in lineage-dependent and lineage-independent manners, whereby interlineage interaction and intralineage retention can redirect cell lineage progression and neuronal subtype generation in the context of disease (Fig. 3E).

Tbx3 deficiency impairs the identity establishment of KNDy but not GnRH neurons

We next performed pairwise transcriptomic comparison of lost neuronal subtypes in NKO mice between our scRNA-seq and snRNA-seq dataset, and found that KNDy neurons represented one of the most robust cell subtypes that were depleted in the central UMS model (Fig. 3F). As aforementioned, KNDy neuronal population acts as a key node controlling the timing of puberty onset by projecting to GnRH nerve terminals (*1*, *2*). To evaluate whether KNDy neurons are completely or partially lost in NKO mice, we performed smFISH with mRNA probes targeting against *Tac2* and *Kiss1* in the ARC nucleus. Our results not only validated the snRNA-seq data showing that early Tbx3 loss completely depleted KNDy neurons in the hypothalamus (Figs. 2, E and I, and 3, G to J) but also corroborated the previous findings that Tbx3 was critical for ARC nucleus specification and fate determination of multiple neuronal subtypes (*26*, *27*). To further investigate the role of Tbx3 in regulating the fate and migration of GnRH neurons, we analyzed their number in rostral preoptic area by smFISH and found that GnRH neurons remained intact in the NKO hypothalamus (Fig. 3, K and L). Collectively, our data support the critical function of Tbx3 in specifying the fate of KNDy neurons but not their downstream target GnRH neurons (Fig. 3M).

Specific deletion of *Tbx3* in KNDy neurons undermines their identity maintenance

There are two distinct steps for dictating the identity of a given cell type: establishment and maintenance (*28*, *29*). Because early ablation of *Tbx3* in the developing hypothalamus revealed that Tbx3 is required for the fate establishment of KNDy neurons (Figs. 2 and 3), we further determined to assess whether Tbx3 also maintains the neuronal identity by using *Tac2-Cre* mouse line to genetically delete *Tbx3* in the postmitotic KNDy neurons. Given the undetectable expression of *Tac2* in early embryonic brains and the specific restriction of *Tbx3* within ARC throughout the brain at late embryonic and postnatal stages, we speculate that Tac2-mediated deletion of *Tbx3* occurs specifically in ARC nucleus (fig. S6). As compared with the poor viability of NKO mice, *Tac2-Cre::Tbx3*$^{Flox/Flox}$ (hereafter referred to as TKO) mice survived into adulthood and displayed normal body weight (Fig. 4, A and B). We subsequently examined the identity maintenance of arcuate KNDy neurons in TKO mice at pre- and peripubertal stages. Our data showed that the number of Tac2- and Kiss1-expressing neurons was notably reduced but not completely depleted in the TKO hypothalamus at P15 (Fig. 4, C to F). The decrement of KNDy neurons was also found at peripubertal stage (P30) in TKO mice, while the number and axonal projection of GnRH neurons were not changed by Tbx3 loss at the same developmental stage (Fig. 4, G and H, and fig. S7, A to D).

To distinguish whether *Tbx3* ablation at neuronal level results in cell loss or peptidergic identity loss, we integrated cell lineage tracing approach with genetic deletion by breeding TKO mice with *Ai140* reporter line to permanently label Tbx3-deficient neurons with green fluorescent protein (GFP). Quantitative analysis of GFP-labeled neurons in ARC indicated that the number of maintained cells was not altered in *Tac2-Cre::Tbx3*$^{Flox/Flox}$*::Ai140* (abbreviated as TKOA) at P0 (Fig. 4, I and J), suggesting that specific *Tbx3* deletion in KNDy neurons does not impair their survival during embryonic development. In contrast, we found a significant decrease in the number of GFP^{+} maintained neurons within the TKOA hypothalamus at P30

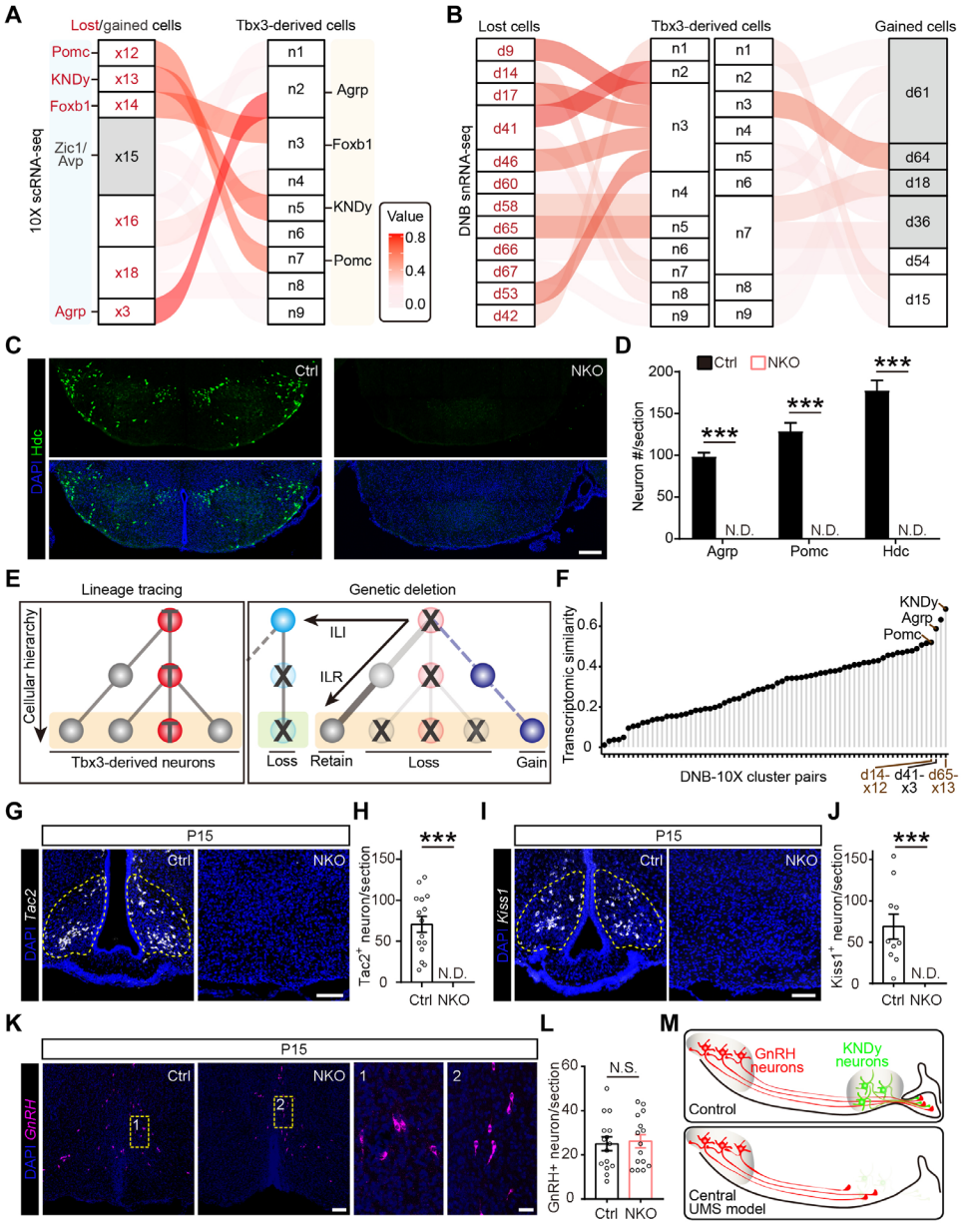

Fig. 3. Tbx3 determines neuronal fate specification in lineage-dependent and lineage-independent manners. (**A** and **B**) Sankey diagrams showing the transcriptomic similarity between lost/gained cell clusters in NKO mice and Tbx3-derived neuronal clusters, as indicated by the Pearson correlation coefficients for each cell type pair from two different datasets. (**C**) Immunostaining shows the ablation of Hdc neurons in the NKO hypothalamus at P15. Scale bar, 200 μm. (**D**) Quantitative analyses of Agrp, Pomc, and Hdc neurons in the control and NKO hypothalamus ($n = 15$ sections from ≥3 mice). N.D., not detected. (**E**) Schematics delineating the lineage progression of Tbx3$^+$ neural progenitors along cellular hierarchy (left) and the neuronal fate remodeling in the absence of Tbx3 (right). ILR, intralineage retention; ILI, interlineage interaction. (**F**) Lollipop chart showing the transcriptomic similarity between the two sets of lost neuronal clusters identified by scRNA-seq and snRNA-seq. (**G** and **H**) Representative images and quantification of arcuate *Tac2*$^+$ neurons in P15 control and NKO mice ($n = 15$ sections from ≥3 mice). Scale bar, 100 μm. (**I** and **J**) Representative images and quantification of arcuate *Kiss1*$^+$ neurons at P15 ($n = 15$ sections from 3 mice). Scale bar, 100 μm. (**K** and **L**) Sample images and quantification of GnRH neurons at P15 ($n = 13$ to 15 sections from 3 mice). Scale bars, 100 and 25 μm. (**M**) Schematic diagram showing the requirement of Tbx3 in specifying the fate of KNDy neurons but not GnRH neurons. ***$P < 0.001$; N.S., not significant by Student's t test.

as compared with controls (Fig. 4, I and J), implicating a partial cell loss during postnatal development. Nevertheless, the viable Tbx3-deficient neurons display a reduced axonal extension into median eminence with minimal projection of axon terminals to the portal vasculature region (fig. S7, E and F). We assume that Tbx3 loss in KNDy neurons may compromise their maturation and integration into neural circuits, and thereby induce cell death in a subpopulation of neurons at postnatal stage.

Unexpectedly, linear regression of the normalized ratio of maintained cells in diverse loss-of-function models implicated that half of the labeled neurons survived in TKOA mice, a quarter of neurons maintained their peptidergic identity in TKO mice, and virtually

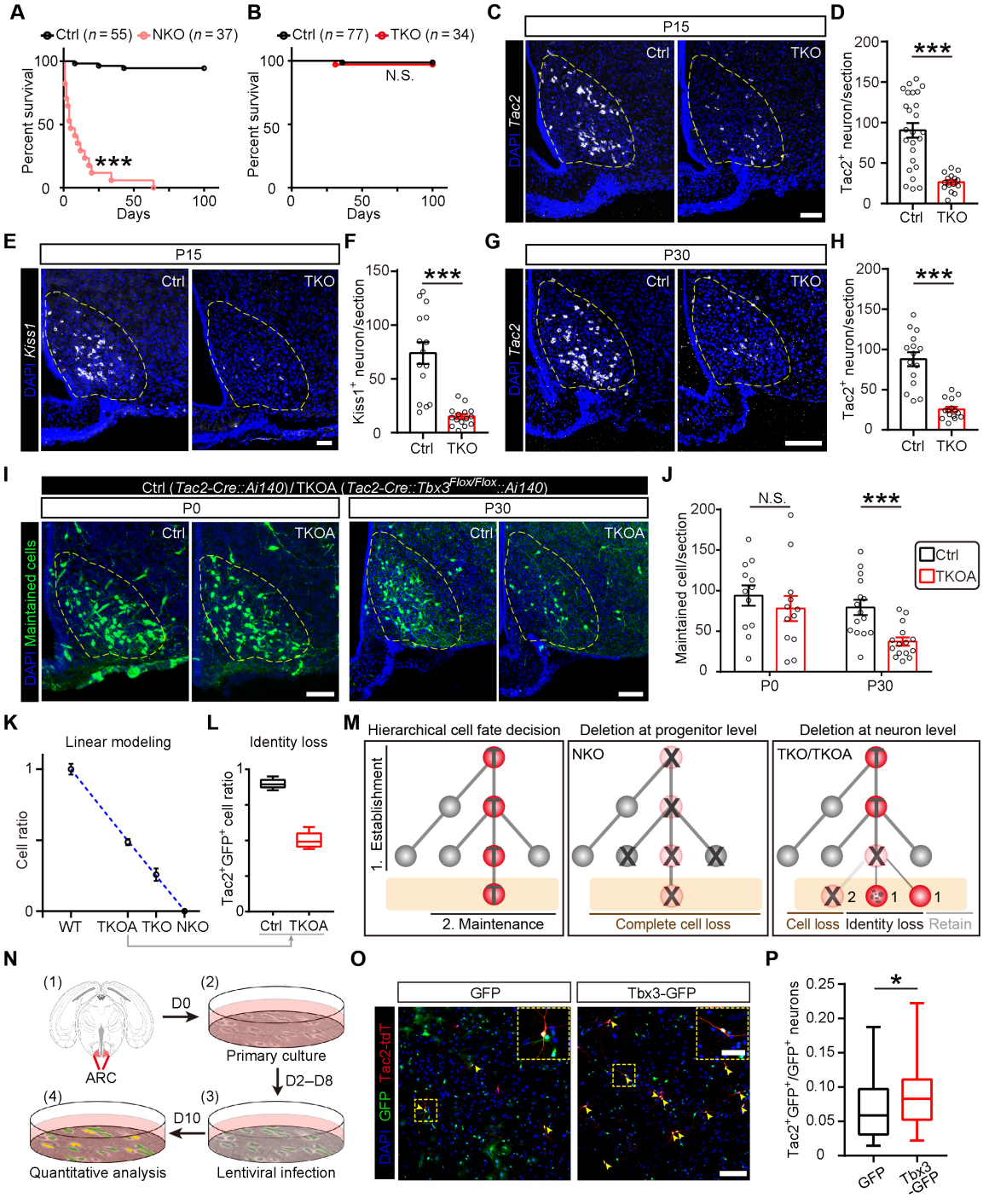

Fig. 4. *Tbx3* deletion at neuronal level undermines the identity maintenance. (**A** and **B**) Kaplan-Meier survival curves of NKO mice (A), TKO mice (B), and their control littermate. Survival curves were compared using the log-rank test. (**C** to **F**) Representative images and quantitative analyses of *Tac2*$^+$ (C and D) and *Kiss1*$^+$ (E and F) neurons in TKO mice at P15 ($n = 15$ to 25 sections from ≥3 mice). Scale bars, 50 μm. (**G** and **H**) Sample images and quantification of arcuate *Tac2*$^+$ neurons at P30 ($n = 15$ sections from 3 mice). Scale bar, 100 μm. (**I** and **J**) Representative images and quantification of Tac2-GFP$^+$ maintained neurons in P0 and P30 ARC ($n = 12$ to 15 sections from 3 mice). Scale bars, 50 and 100 μm. (**K**) Linear modeling of the relative ratio of retained KNDy neurons that lost their neuropeptide identity or not in NKO, TKO, and TKOA mice. (**L**) Quantification of the percentage of GFP$^+$ viable cells expressing *Tac2* in P30 ARC ($n = 3$). (**M**) Model diagrams depicting the hierarchical cell fate decision of NPCs, and the role of Tbx3 in neuronal identity establishment and maintenance. (**N**) An experimental pipeline showing the procedure of neuronal fate induction in vitro. (**O**) Representative images showing the increased number of Tac2-tdT$^+$ neurons following Tbx3 overexpression. Scale bars, 150 and 50 μm. (**P**) Quantification of the ratio of Tac2-tdT$^+$GFP$^+$ neurons among infected neuronal populations ($n = 41$ to 46 fields of view). *$P < 0.05$; ***$P < 0.001$; N.S., not significant by Student's *t* test.

none of KNDy neurons existed in NKO mice (Fig. 4K). To validate our linear modeling and align the data collected from TKOA and TKO brains with different readouts, we further analyzed the number of Tac2-expressing neurons in P30 TKOA mice and found that only half of GFP^+ surviving neurons within ARC expressed Tac2 neuropeptide in the context of Tbx3 deficiency (Fig. 4L and fig. S7, G and H). These data suggest that *Tbx3* ablation at progenitor level with *Nkx2.1-Cre* line abolishes both identity establishment and maintenance of KNDy neurons, whereas genetic deletion at neuronal level with *Tac2-Cre* line only impairs cell identity maintenance, leading to neuronal death, peptidergic identity loss, and neuronal retention in a ratio of 2:1:1 (Fig. 4M).

Furthermore, we performed primary culture of arcuate neurons from the embryonic *Tac2-Cre::Ai9* mice, wherein tdTomato expression reflects the identity of KNDy neurons, and overexpressed Tbx3 in these neurons by lentiviral infection (Fig. 4N and fig. S7, I and J). At 10 days after in vitro culture, we analyzed the ratio of Tac2-expressing neurons among the infected cell population and found that Tbx3 overexpression increased the number of $tdTomato^+$ neurons (Fig. 4, O and P). Nevertheless, we could not induce the transdifferentiation of nonarcuate neurons into Tac2 neurons by ectopic expression of Tbx3 (fig. S7, K and L), which may require the removal of a potential epigenetic barrier. Together, our results suggest the necessity and sufficiency of Tbx3 to enhance the fate specification of KNDy neurons in ARC nucleus.

Identity maintenance of KNDy neurons is critical for puberty onset

As aforementioned, UMS patients carrying *TBX3* mutations frequently display delayed puberty onset and genital hypoplasia (*14*, *20*). To determine whether Tbx3 loss of function in KNDy neurons recapitulates the phenotypes observed in UMS patients, we analyzed the timing of puberty onset and performed fertility assay in male and female TKO mice. In males, genetic ablation of *Tbx3* resulted in a marked delay in puberty onset, as observed by preputial separation (Fig. 5, A and B). Although female TKO mice exhibited a subtle delay in the timing of vaginal opening, they failed to reach sexual maturation, as determined by the lack of ovulation (Fig. 5, C and D, and fig. S8, A and B). Temporal analysis of serum luteinizing hormone (LH) levels indicated that there emerged a surge in basal LH concentration in wild-type (WT) females around the puberty onset, but *Tbx3* deletion in KNDy neurons disrupted the LH surge in female mice for initiating puberty (fig. S8C). Daily inspection of vaginal cytology for 30 days during adulthood further showed an absence of estrous cyclicity in female TKO mice, trapped at the metestrus/diestrus phases without an entry into estrus (Fig. 5, E and F, and fig. S8, D to F). Given the lack of estrus cyclicity in female TKO mice, we assessed their fertility by exposing them to fertile WT males for 90 days and found that all TKO mice failed to conceive and deliver a litter of pups (Fig. 5G).

To examine the potential genital hypoplasia in TKO mice, we collected testes from males and ovaries from females for morphological analysis. In males, the size and weight of testes were significantly reduced in TKO mice as compared with control and heterozygous mice (Fig. 5, H and I). Female TKO mice also showed a marked reduction in the size and weight of ovaries (Fig. 5, J and K), and ovarian histological analysis further indicated that corpora lutea were barely detectable in the absence of Tbx3 in KNDy neurons (Fig. 5L). To exclude the potential ablation of *Tbx3* in the gonads of TKO mice and its direct consequence of gonad dysfunction, we analyzed the gene expression in P30 gonads and found that the abundance of *Tbx3* was not altered in the TKO ovaries as compared to controls (fig. S8G), while the expression level of *Tbx3* was extremely low in both control and TKO testes (fig. S8H). Further staining and single-cell analyses not only corroborated the low expression of *Tbx3* in mouse testes but also demonstrated that the expression of *Tbx3* and *Tac2* did not overlap in the same cell types from ovaries of juvenile and adult mice (fig. S8, I to K) (*30*, *31*). These results support the central regulation of gonadal maturation by hypothalamic KNDy neurons. Given that KNDy neurons have been implicated in the control of energy balance (*1*), we monitored the body weight gain of TKO mice during development but found that the overall body weight of both male and female mice was not changed by genetic abrogation of *Tbx3* (fig. S8, L and M). Together, these results demonstrate that the identity maintenance of KNDy neurons is critical for puberty onset and reproductive capacity but not energy homeostasis in mammals, and suggest that the impaired sexual maturation in UMS patients can be modeled with conditional *Tbx3* knockout mice.

Tbx3 proteins form phase-separated condensates

Dynamic compartmentalization of transcription factors by phase-separated condensates regulates the assembly and activity of transcriptional machinery at genomic loci (*32*). High-resolution imaging revealed that endogenous mouse Tbx3 proteins (mTbx3) localized to nuclear punctate structure in the ESCs and their derived hypothalamic progenitors (Fig. 6A). In the primary cultured neurons from mouse embryonic hypothalamus, we also observed a partition of mTbx3 into subnuclear puncta, which was completely lost in Tbx3-deficient neurons (Fig. 6A and fig. S9A). Next, we proceeded to assess whether mTbx3 spontaneously assembles into condensates in vivo, and found the same punctate structures in the nuclei of neural progenitors and neurons within the developing mouse hypothalamus (Fig. 6B and fig. S9B). These results implicate the phase separation of mTbx3 in executing its physiological functions, regardless of the cell types observed. To validate its biophysical properties, we cloned the gene encoding human TBX3 (hTBX3) that shared 93.2% identical amino acid residues with its mouse homolog and contained long segmented stretches of intrinsically disordered regions (IDRs) (fig. S9C), purified the recombinant proteins, and performed in vitro phase separation assays at different protein and salt concentrations. Under these conditions, there were three distinguishable biophysical states: irregular aggregates, phase-separated condensates, and soluble molecules, depending on the ionic strength of buffer. We optimized the salt concentration and found that fluorescently labeled hTBX3 started to form visible phase-separated droplets at a concentration of 10 μM in a buffer with 180 mM NaCl (Fig. 6C and fig. S9D). The proteins assembled into irregular aggregates at lower salt concentration but dissolved into diffusible molecules with higher ionic strength, and the abundance of these condensates augmented with the increase of protein concentration (Fig. 6C). To assess the dynamic property of hTBX3, we further conducted fluorescence recovery after photobleaching (FRAP) analysis by bleaching the center of condensates and monitoring the fluorescence recovery, which revealed that approximately 50% of the hTBX3 signal intensity recovered within 12 min after bleaching (Fig. 6, D and E, and movie S4). In contrast, the fluorescence recovery in the solid aggregates was lacking at lower salt concentration (fig. S9E). These data collectively indicate that hTBX3

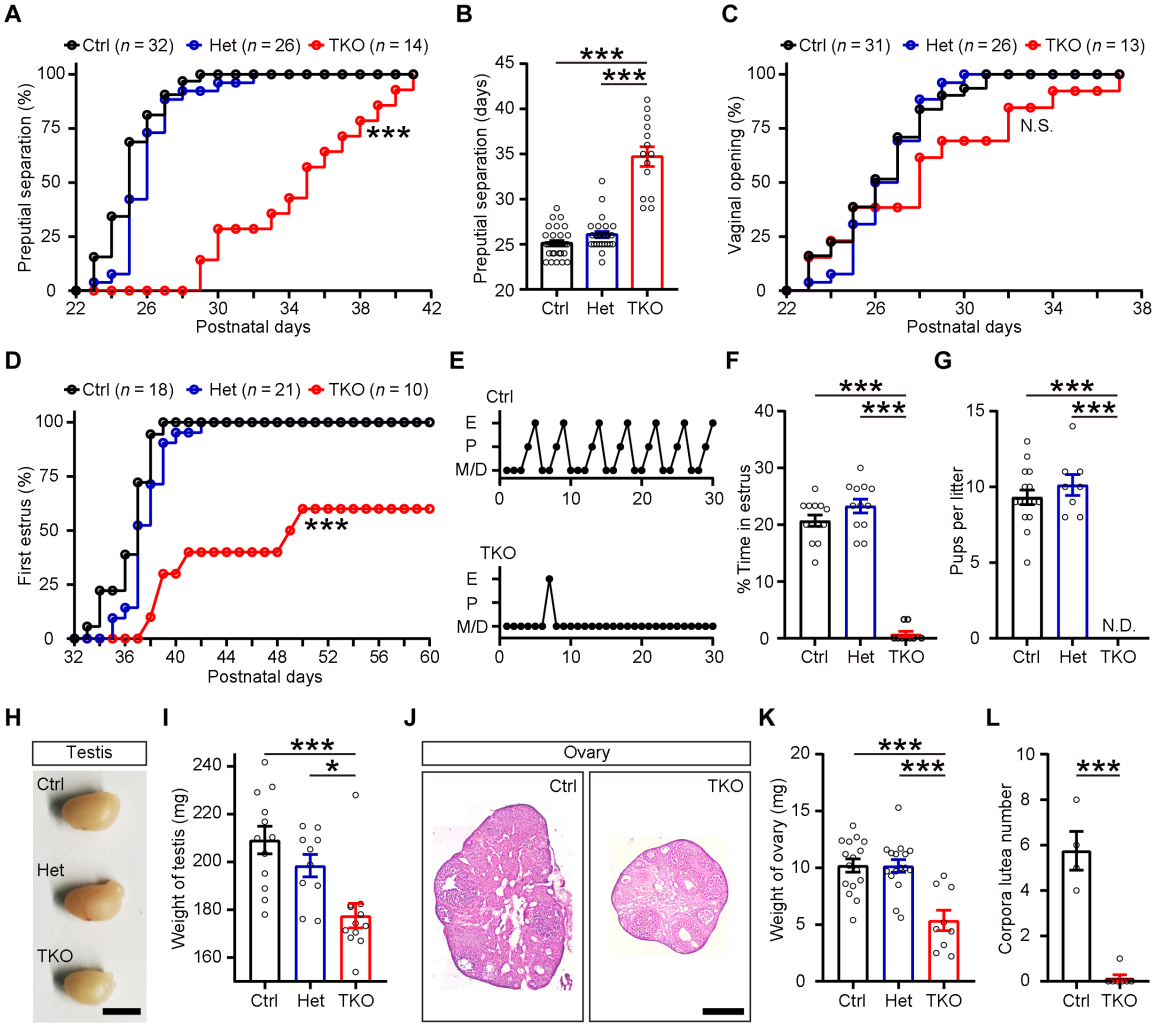

Fig. 5. Tbx3 loss in KNDy neurons causes abnormal puberty onset and reproductive defects. (**A**) Cumulative percentage of male mice with preputial separation. Het, heterozygous. (**B**) Bar plot showing the average age of preputial separation in male mice. (**C**) Cumulative frequency graph showing the age of female mice with vaginal opening. (**D**) Cumulative percentage of female mice with first estrus determined by vaginal cytology. (**E**) Estrus cycle profiles showing the lack of estrus cyclicity in TKO mice, determined by daily vaginal cytology for 30 days. E, estrus phase; P, proestrus phase; M/D, metestrus/diestrus phases. (**F**) Bar plot showing the percentage of time spent in estrus phase for female mice ($n = 13$, 12, and 9 for control, heterozygous, and TKO groups, respectively). (**G**) Quantification of the number of pups delivered by female mice ($n = 16$, 8, and 10 for control, heterozygous, and TKO groups, respectively). (**H**) Representative photograph showing the testis histomorphology in male mice. Scale bar, 5 mm. (**I**) Bar graph showing the average weight of testis ($n = 12$, 10, and 12 for control, heterozygous, and TKO groups, respectively). (**J**) Hematoxylin and eosin staining shows the ovarian histology in female mice. Scale bar, 400 μm. (**K**) Quantification of the weight of ovary ($n = 16$, 16, and 9 for control, heterozygous, and TKO groups, respectively). (**L**) Quantitative analysis of the number of corpora lutea in ovaries of female mice ($n = 4$ and 7 for control and TKO groups, respectively). $^*P < 0.05$; $^{***}P < 0.001$; N.S., not significant by one-way ANOVA or Student's *t* test.

can undergo phase separation with liquid-like behavior, which is sensitive to salt concentrations.

Pathogenic hTBX3 mutations disturb the phase separation of encoded proteins and their transcriptional regulation

Recent studies suggest that phase separation of transcription factors could provide a critical biophysical basis for the transcriptional control of gene expression (*33*, *34*). To gain insight into the molecular pathological mechanism of delayed puberty in UMS patients, we selected four genetic variants of *TBX3* associated with impaired sexual maturation in human beings for further phase separation analysis (*14*, *20*, *35*). Among the selected genetic mutations, three of them (L143P, Y149S, and S190R) occurred in T-box domain that is evolutionarily conserved in different species, and the other nonsense mutation (Q475X) introduced a termination codon in the activation domain of hTBX3 (Fig. 6F and fig. S9, F and G). We constructed a series of plasmids encoding hTBX3 with point or truncated mutations to mimic the disease-causing genetic variants, purified these proteins, and analyzed their biophysical properties. Our data showed that all of these mutant proteins could not appropriately form phase-separated condensates at optimal salt concentration (Fig. 6G), suggesting that the pathogenic mutations in *TBX3* might disturb its protein folding and phase separation needed for driving proper transcriptional regulation.

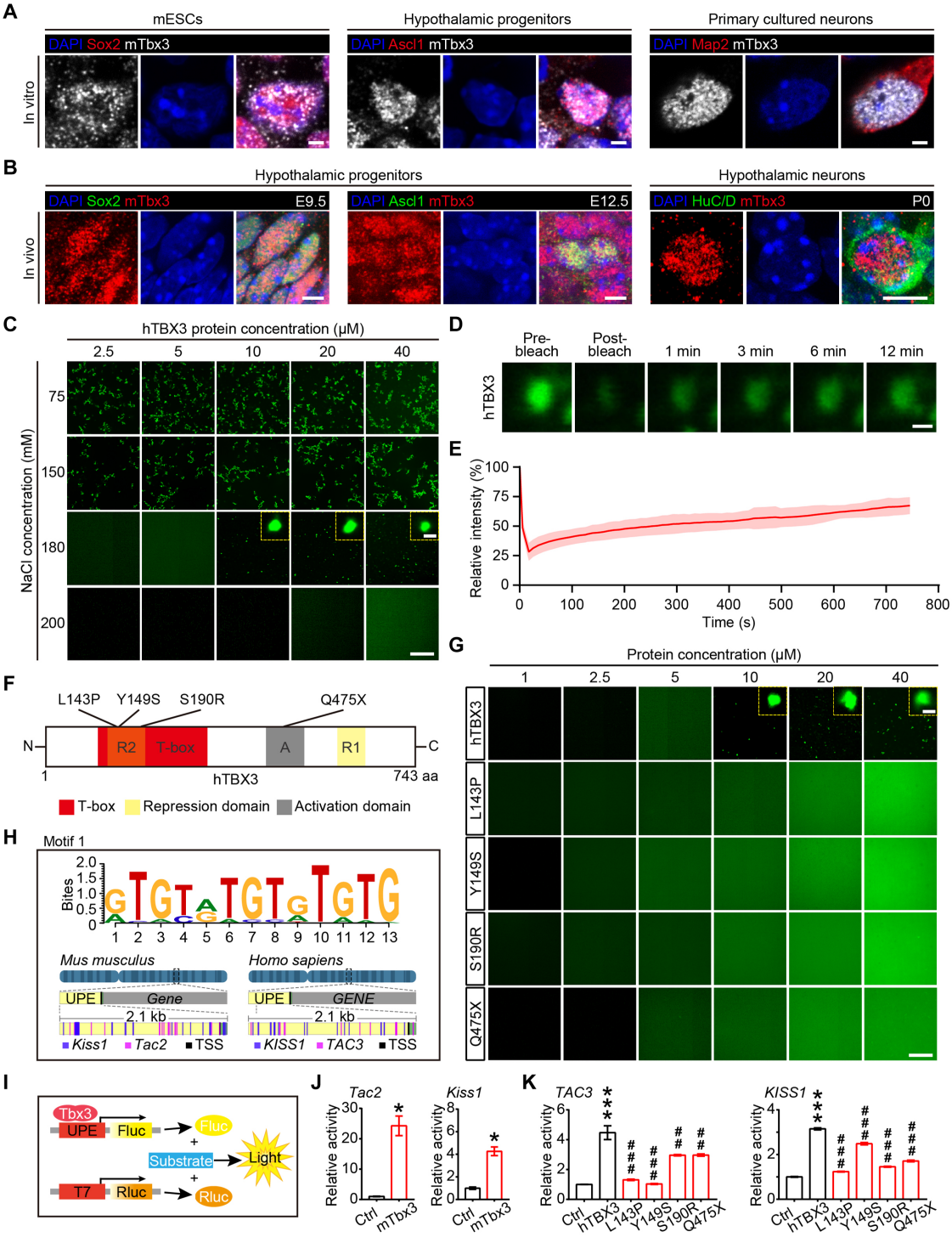

Fig. 6. hTBX3 undergoes phase separation and regulates specific transcriptional events. (**A**) Confocal microscopy images showing the punctate structure of mTbx3 in mESCs, mESC-derived hypothalamic progenitor cells, and primary cultured neurons. Scale bars, 2 μm. (**B**) High-resolution confocal images showing the mTbx3 puncta distributed in the nuclei of hypothalamic progenitors and neurons. Scale bars, 4 μm. (**C**) Phase diagram of recombinant hTBX3 protein at different protein and salt concentrations ($n = 3$). Scale bars, 20 and 1 μm. (**D**) FRAP assay showing the fluorescent recovery of hTBX3 signal after photobleaching with high-intensity laser. Scale bars, 500 nm. (**E**) Quantification of FRAP assays for hTBX3 droplets ($n = 6$). (**F**) Schematic diagram of the structural domains within hTBX3. (**G**) Phase diagram of hTBX3 and its disease-causing mutants at the salt concentration of 180 mM. Scale bars, 20 and 1 μm. (**H**) Graphic diagram showing the sequence logo of representative mTbx3 binding motif and the Tbx3 binding sites in the upstream promoter element (UPE) of *Tac2*/*TAC3* and *Kiss1*/*KISS1* genes. TSS, transcription start site. (**I**) Simplified workflow of luciferase assay. Fluc, firefly luciferase; Rluc, renilla luciferase. (**J**) Quantification of the normalized luciferase activity indicating that mTbx3 activates mouse *Tac2* and *Kiss1* genes in HEK293T cells ($n = 3$; $^{*}P < 0.05$ by Student's *t* test). (**K**) Bar plots showing the promoter activity of human *TAC3* and *KISS1* regulated by hTBX3 and its pathogenic mutants ($^{***}P < 0.001$ versus control group; $^{\#\#}P < 0.01$; $^{\#\#\#}P < 0.001$ versus hTBX3 group by one-way ANOVA).

Furthermore, we extended the structural assessment of hTBX3 mutants to functional analysis by evaluating the transcriptional regulation of signature gene expression in KNDy neurons. To assess the potential regulatory role of mTbx3 on *Tac2* and *Kiss1* expression, we first performed CUT&Tag (cleavage under targets and tagmentation) assay, inferred the mTbx3 binding motif using the motif discovery program MEME together with JASPAR analysis of public database (see Materials and Methods), and revealed that the putative promoters of *Tac2* and *Kiss1* genes were enriched with the identified GTGT motif (Fig. 6H; fig. S9, H to J; and table S5; see Methods). Luciferase assay with a 2.1-kb promoter upstream of the translation start sites (TSSs) showed that overexpression of mTbx3 in human embryonic kidney (HEK) 293T cells significantly enhanced the promoter activity of both *Tac2* and *Kiss1* genes (Fig. 6, I and J). We also found an enrichment of GTGT motif in the promoters of human *TAC3* (homologous to mouse *Tac2*) and *KISS1* genes, and a robust stimulatory action of hTBX3 on these promoters (Fig. 6, H and K, and fig. S9, H to J). Consistent with the disturbed phase separation of mutant proteins, hTBX3-mediated transcriptional activation of *TAC3* and *KISS1* was significantly attenuated by the pathogenic mutations identified in UMS patients (Fig. 6K). These results suggest that *TBX3* mutations may disrupt puberty onset in UMS patients by impairing the phase separation of encoded proteins and their transcriptional regulation of key neuropeptides in KNDy neurons.

DISCUSSION

For decades, Waddington's concept of the "epigenetic landscape" has served as an educative hierarchical model to illustrate the progressive restriction of cell differentiation potential during normal development (*36*). In the hypothalamus, we have recently revealed a cascade diversification strategy adopted by progenitors and precursors along the cell lineage hierarchy for generating extreme neuronal diversity (*26*). Within the cell lineage tree, the differentiation of a specific cell subtype may require a progressive restriction of cell fate. Here, we identified Tbx3 as a critical transcription factor with a broad-to-restricted expression pattern in the developing hypothalamus, which sequentially directed the identity establishment and maintenance of KNDy neurons. We then used an unprecedented strategy of cell type alignment by comparing single-cell datasets from lineage tracing and genetically manipulated mice, and revealed the rules of interlineage interaction and intralineage retention during cell fate specification, extending the well-recognized lineage-dependent mechanism. Moreover, our study uncovered the cellular and molecular mechanisms underlying how *TBX3* mutations interfere with the onset of puberty in UMS patients.

Hierarchical regulation of neuronal fate by a T-box transcription factor

Great efforts have been made in the past two decades to elucidate the genetic programs underlying the fate determination of neurons and generation of neuronal diversity in central nervous system (*37*–*39*). Different transcription factor families have been found to serially control distinct steps in the differentiation of neural progenitor cells into neurons, ranging from neural patterning, progenitor specification, proneural induction, neuronal identity establishment, and maintenance (*15*, *40*). For example, homeobox proteins such as Pax6, Nkx2.1, and Rax regulate the patterning of neural primordium in different brain regions, whereas basic helix-loop-helix proteins such as Ascl1 and Neurog2 act as proneural genes to drive neuronal differentiation and contribute to neuronal identity establishment (*15*, *41*–*43*). However, little is known about the role of T-box family in neuronal fate acquisition and specification. As a representative of T-box family, Tbx3 defines a progenitor domain in the hypothalamic primordium and displays a broad-to-restricted expression pattern throughout the developmental continuum, implicating its involvement in the whole process of neuronal differentiation. With the progression of neuronal lineage, Tbx3 first functions as a patterning gene to define the primordium of acroterminal hypothalamus and loss of Tbx3 disrupts nucleus formation and organization. Second, Tbx3 activates region-specific differentiation programs in neural progenitors and controls the fate specification of multiple neuronal subtypes with lineage-dependent and lineage-independent mechanisms. The fact that Ghrh neurons derived from Tbx3 lineage are retained but Hdc neurons arising from another Tbx3-independent lineage are eliminated allows us to propose the rules of intralineage retention and interlineage interactions for regulating cell fate specification, although how the defect in the development of one cell lineage alters the cell differentiation in another independent lineage remains an open issue. Last, Tbx3 expression persists in a set of postmitotic neuronal subtypes and maintains their identity in postnatal brains, supported by a recent study showing that the identity maintenance of melanocortin neurons depends on Tbx3 (*21*). These results collectively demonstrate that the T-box transcription factor Tbx3 establishes and maintains the fate of specific neuronal subtypes in a hierarchical manner.

Although it has previously been shown that the transcription factors that initiate neuronal fate acquisition may also maintain their neurotransmitter identity (*16*, *44*), to what extent targeted disruption of these factors in postmitotic neurons causes identity loss and cell loss remains unclear. Our study combined smFISH, single-cell analysis, and fate mapping to provide compelling evidences showing that genetic deletion of *Tbx3* in KNDy neurons leads to the death of ~50% cells, identity loss of ~25% cells, and retention of ~25% cells. Whether Tbx3 is exclusively required for the survival of KNDy neurons or whether the neuronal loss is a secondary consequence of neuropeptide identity loss requires further investigation.

The requirement of KNDy neuronal identity for puberty onset

Although previous studies show that germline knockout of kisspeptin or tachykinins (encoded by *Tac1* and *Tac2*) in mice leads to delayed puberty onset (*45*, *46*), the physiological functions of KNDy neurons and the neuropeptides they express in regulating the timing of puberty onset remain controversial. Notably, it was reported that congenital ablation of kisspeptin neurons (including KNDy population) in the hypothalamus did not impair puberty onset in female mice (*47*), suggesting that developmental compensation of other reproductive neural circuits might occur to restore the timing of puberty onset in the complete absence of kisspeptin neurons. Furthermore, the initiation of puberty is well preserved in mice with specific ablation of *Kiss1* in KNDy neurons (*48*), whereas conditional deletion of *Nhlh2* causes a significant decrease in the *Kiss1* expression within KNDy neurons and subtly delays the preputial separation of male mice, but does not impair the onset of puberty in female mice (*49*). Here, we demonstrate that loss of most but not all KNDy neurons, induced by conditional knockout of *Tbx3*, is

sufficient to delay the timing of puberty onset in both male and female mice. Combined with previous reports, our study suggests that delayed puberty onset could be caused by the cumulative effect of reduced KNDy neuronal number and neuropeptide identity loss. On the basis of the hypothesis that arcuate kisspeptin enhances pubertal progression to reach the point of adult-pattern GnRH pulsatility rather than initiates puberty (*48*), we speculate that neurokinin B in KNDy neurons may dominate over kisspeptin to trigger puberty onset.

Pathological mechanisms underlying the delayed puberty in UMS patients

In humans, *TBX3* mutations have been linked to UMS, which is characterized by forelimb defects, mammary gland hypoplasia, genital abnormalities, obesity, short stature, decreased fertility, and delayed puberty (*19*, *50*). Although it has previously been explored how Tbx3 regulates the development of forelimb and mammary gland (*51*–*53*), the cellular and molecular mechanisms underpinning neuroendocrine disorders (e.g., delayed puberty and gonadal failure) in UMS patients remain enigmatic. Here, we show that loss of most KNDy neurons in *Tbx3* conditional knockout mice leads to delayed puberty, deficient fertility, and reduced gonad size. At the molecular level, we reveal that pathogenic *TBX3* mutations identified in UMS patients disturb the phase separation of encoded proteins and subsequently impair their transcriptional regulation of *TAC3* and *KISS1*, which shape the identity and regulate the activity of KNDy neurons in mammals. Among the pathogenic mutations associated with UMS, there are five nonsense (K273X, Q331X, S343X, Q360X, and Q475X) and three missense (L143P, Y149S, and S190R) mutations within *TBX3* (*14*, *18*). Most nonsense mutations occur in the predicted IDR of hTBX3, implicating that these truncated mutations may alter the phase separation property of encoding proteins. Our data corroborate that Q475X encoding the longest truncation variant among the nonsense mutants fails to form phase-separated condensate in vitro. In contrast, all three missense mutations occur in the T-box domain but not IDR of hTBX3, presumably compromising their DNA binding affinity. Nevertheless, our structural analysis shows that the three amino acid residues (L143, Y149, and S190) susceptible to missense mutation are close with each other in the context of three-dimensional conformation and, unexpectedly, distal from both DNA binding region and dimerization interface. Given our results showing the impaired phase separation of these missense mutants, it is possible that the UMS-causing missense mutations disrupt the correct conformation of T-box domain, destabilize the protein folding of hTBX3, and thereby hamper its phase separation, which consequently causes the transcriptional regulatory inactivation.

Together, our study systematically reveals Tbx3-derived neuronal lineage and Tbx3-mediated neuronal specification, and the rules of interlineage interaction and intralineage retention during neuronal differentiation. More specifically, we propose a Tbx3-dependent hierarchical fating mechanism operating within the lineage to generate KNDy neurons and uncover the molecular pathological mechanism underlying the delayed puberty onset in UMS patients caused by *TBX3* mutations.

MATERIALS AND METHODS

Animals

Rax-CreER^{T2} (stock no. 025521) and *Ai9* (stock no. 007909) were obtained from the Jackson Laboratory. *Nkx2.1-Cre* (stock no. 008661), *Tac2-Cre* (stock no. 018938), *Ai140* (stock no. 030220), and *Tbx3$^{Flox/Flox}$* mouse lines were provided by Z. Yang, X. Xu,. H. Zeng, and A. Moon's laboratories, respectively. WT C57BL/6N mice at the age of E10.5, E12.5, E14.5, and P0 were ordered from SPF Biotechnology Co. Ltd. (Beijing, China) for brain tissue collection. We further bred *Nkx2.1-Cre::Tbx3$^{Flox/Flox}$* (NKO), *Tac2-Cre::Tbx3$^{Flox/Flox}$* (TKO), and *Tac2-Cre::Tbx3$^{Flox/Flox}$::Ai140* (TKOA) mice for this study. Animals were maintained on a 12-hour light/12-hour dark cycle at a temperature of 21°C with 50 to 60% humidity and provided with food and water ad libitum. All animal procedures used in this study were performed according to protocols approved by the Institutional Animal Care and Use Committee at Institute of Genetics and Developmental Biology, Chinese Academy of Sciences.

Cultured cells

HEK293T cells were cultured in Dulbecco's modified Eagle's medium (DMEM) (Gibco) supplemented with 10% fetal bovine serum (FBS) (HyClone). Mouse embryonic stem cells (mESCs; E14TG2a, American Type Culture Collection) were maintained in medium containing DMEM supplemented with 15% FBS, 1× non-essential amino acids (NEAA) (Gibco), 1× GlutaMAX (Gibco), 1× sodium pyruvate (Gibco), 0.1 mM β-mercaptoethanol (Gibco), 3 μM CHIR99021 (Stemolecule), 1 μM PD 0325901 (Stemolecule), leukemia inhibitory factor (LIF) (1000 U/ml; Millipore), penicillin (50 U/ml), and streptomycin (50 mg/ml). To obtain hypothalamic progenitors from mESCs, we transferred the dissociated mESCs into DMEM/F12 (Gibco) medium containing 1× N2 (Gibco) and 1× B27 (Gibco) using 96-well low cell adhesion plates. On the second day after differentiation, we treated the cells with 600 nM sonic hedgehog (SHH) (BioLegend) and 2.5 nM IWR-1-endo (Cayman) to induce the differentiation of mESCs into hypothalamic progenitors. The cells were cultured at 37°C in a humidified incubator with 5% CO_2.

Plasmids

To construct lentiviral plasmids, we amplified the coding sequence of mouse *Tbx3* and cloned into lentiviral vector pCDH–cytomegalovirus (CMV) using the In-Fusion HD Cloning Kit (Clontech, #639649). For in vitro phase separation assays, human TBX3 and its truncation mutant (Q475X) were amplified and cloned into pRSFDuet vector with an N-terminal myelin basic protein (MBP) tag and C-terminal 8× His tag using the ClonExpress II One Step Cloning Kit (Vazyme, #C112-01). Plasmids encoding TBX3 with missense mutations (L143P, Y149S, and S190R) were generated by site-directed mutagenesis. The pGL3-basic vector (#E1751) encoding firefly luciferase and pRL-TK vector (#E2241) expressing renilla luciferase were purchased from Promega Corporation. We amplified the 2.1-kb DNA fragments upstream of the TSS of mouse *Tac2*, mouse *Kiss1*, human *TAC3*, and human *KISS1* genes and cloned into pGL3-basic vector for luciferase assay.

Generation of *Tbx3-CreER^{T2}* mouse strain

To assess the expression pattern of Tbx3 and trace the lineage of Tbx3^{+} neural progenitors with precise temporal resolution, we determined to generate an inducible *Tbx3-CreER^{T2}* knock-in mouse line, in which the first exon of *Tbx3* gene was partially replaced by a DNA fragment encoding tamoxifen-inducible Cre recombinase. We first designed a gene-targeting donor vector containing CreER-poly(A)-Frt-PGK-Puro-Frt cassette that was flanked by the 5′ untranslated region and the first intron of *Tbx3* locus. The donor

vector was linearized and then electroporated into mESCs with pX330 vector encoding both Cas9 and single-guide RNAs at a ratio of 3:2 (w/w) using Nucleofector 2b Device (AAB-1001, Lonza). The electroporated mESCs were treated with puromycin (2 μg/ml) for 3 days, and the positive colonies were manually selected for further validation. Subsequently, the *Tbx3-CreER^{T2}* mESC lines with correct genotype and karyotype were injected into the mouse blastocyte-stage embryos to generate chimeric mice, which were used to breed with WT C57BL/6N mice for passing the positive mESC-derived gametes to the next generation. In the knock-in mouse line, the *CreER^{T2}* sequence was inserted six nucleotides downstream of the in-frame start codon of the endogenous *Tbx3* locus.

We confirmed germline transmission of the *Tbx3-CreER^{T2}* targeted locus and found that the heterozygous *Tbx3-CreER^{T2}* mice were viable and fertile without any obvious gross abnormalities. To assess tamoxifen-inducible Cre activity, we crossed *Tbx3-CreER^{T2}* knock-in mice with *Ai9* reporter mice that expressed tdTomato after Cre-mediated recombination. A robust tdTomato expression enhanced by immunostaining was observed in tamoxifen-treated *Tbx3-CreER^{T2}::Ai9* mice, while leaky fluorescence was not detected in untreated mice.

Lineage tracing and three-dimensional reconstruction

To genetically label Tbx3$^+$ neural progenitors and their progeny cells, we bred *Tbx3-CreER^{T2}* mice with *Ai9* reporter mice, checked the vaginal plug to determine the time of pregnancy, and intraperitoneally injected a single dose of tamoxifen (132 mg/kg body weight) into pregnant dams at E9, E11, and E13 to label Tbx3$^+$ hypothalamic progenitors in the embryonic brains. Mouse embryos at E14 were obtained by cesarean section and perfused intracardially with cold 4% paraformaldehyde (PFA) in phosphate-buffered saline (PBS) before postfixation, while E10 embryos were collected for direct fixation with 4% PFA. To collect postnatal brains, we recovered live embryos at E18 and E19 by cesarean section, cared the pups with foster female animals, and sacrificed the postnatal mice for further analyses. The brains derived from E10, E14, P0, P14, and P21 *Tbx3-CreER^{T2}::Ai9* mice were serially sectioned, immunostained, and imaged using Zeiss or Leica confocal microscopy.

For three-dimensional reconstruction, optical stacks of images were serially aligned along the rostrocaudal axis using Reconstruct 1.1.0 (J.C. Fiala, National Institutes of Health), followed by importing into Imaris 9.0 (Bitplane) for further analyses. In the reconstructed brains, we created "surfaces" by outlining the brain and diencephalon contour and "spots" for each genetically labeled cells.

Single-cell isolation and scRNA-seq

We isolated single cells from *Tbx3-CreER^{T2}::Ai9* mice as previously described (*26*). Specifically, we labeled Tbx3$^+$ progenitors by three intraperitoneal tamoxifen injections at E9, E11, and E13 into *Tbx3-CreER^{T2}::Ai9* mice, collected P12 brains, and microdissected hypothalamus under a fluorescence stereomicroscope (Lecia M205, Leica Microsystems, Germany). The hypothalamic tissues were transferred into a 5-ml Eppendorf tube and treated with digestion buffer for 1.5 hours at 37°C. The digestion was terminated by replacing the buffer with Hibernate A buffer containing 1× GlutaMAX, 0.05 mM D,L-2-amino-5-phosphonovaleric acid, 0.2× B27, 0.01 mM Y27632 dihydrochloride, and 1% FBS. The tissues were then gently triturated through Pasteur pipettes with finely polished tips and washed once with Hibernate A buffer to generate single-cell suspension. Subsequently, the dissociated hypothalamic cells were stained with 4′,6-diamidino-2-phenylindole (0.2 μg/ml) for the exclusion of dead cells and subjected to FACS (BD FACSAria II flow cytometer, BD Biosciences, USA) for isolating tdTomato-positive live cells. The single-cell isolation method was also applied for preparing single-cell suspensions from P14 NKO mice.

scRNA-seq libraries were constructed according to the instructions provided by 10× Genomics accompanying the single-cell 3′ Library and Gel Bead Kit V3 (10× Genomics, 1000075). Single-cell suspensions (300 to 600 living cells/μl determined by Count Star) were loaded on the Chromium Single Cell Controller to generate single-cell gel beads in the emulsion (GEM). Captured cells were lysed to release mRNA, which were subsequently barcoded by reverse transcribing individual GEMs. Using the S1000TM Touch Thermal Cycler (Bio-Rad, USA) to reverse transcribe, the GEMs were programmed at 53°C for 45 min, followed by 85°C for 5 min and hold at 4°C. The complementary DNA (cDNA) library was then generated, amplified, and assessed for quality control using Agilent 4200. scRNA-seq was further performed on the Illumina NovaSeq 6000 sequencer with a sequencing depth of at least 100,000 reads per cell and 150–base pair (bp) paired-end reads.

Immunohistochemistry and immunocytochemistry

The mice were transcardially perfused with 4% PFA in 1× PBS under anesthetic (400 mg/kg of 2,2,2-tribromoethanol), followed by the immediate dissection of mouse brains for postfixation in 4% PFA. The mouse brains were then cryoprotected in 20 or 30% sucrose solution for 24 hours, embedded in Tissue-Tek O.C.T. Compound (Sakura 4583), and cut into sections (20 to 40 μm in thickness) with a cryostat microtome (Leica, CM3050S). For immunostaining, brain sections were washed with 1× PBS, preblocked with 1× TBS++ (pH 7.4, containing 3 mM KCl, 25 mM Trizma base, 137 mM NaCl, 5% donkey serum, and 0.3% Triton X-100) for 1 hour at room temperature (RT), and then incubated with primary antibodies in 1× TBS++ overnight at 4°C. The primary antibodies in this study included rabbit anti-Tbx3 (Abcam, ab99302; 1:400), rabbit anti–red fluorescent protein (Rockland, 600-401-379; 1:800), goat anti-mCherry (Biorbyt, orb11618; 1:800), rabbit anti-Nkx2-1 (Abcam, 76013; 1:250), goat anti-Sox2 (R&D Systems, AF2018; 1:400), mouse anti-Ascl1 (BD Biosciences, 556604; 1:250), mouse anti-Neurog2 (R&D Systems, MAB3314; 1:250), mouse anti-HuC/D (Invitrogen, A21271; 1:400), goat anti-Foxb1 (Abcam, ab5274; 1:400), rabbit anti-Otp (GeneTex, GTX119601; 1:400), rabbit anti-GnRH (Abcam, ab281844; 1:400), rabbit anti-Hdc (Progen, 16045; 1:400), rabbit anti-Pomc (Phoenix Pharmaceuticals, H-029-30), and rabbit anti-Nr5a1 (Cosmo Bio, KO611). After primary antibody incubation, the tissue sections were washed for three times with 1× PBS and incubated with secondary antibodies for 2 hours at RT, which included anti-goat Cy2, anti-rabbit Cy2, anti-goat Cy3, anti-rabbit Cy3, and anti-rabbit Cy5 (donkey, Jackson ImmunoResearch; 1:500).

For immunocytochemistry, cultured cells on round cover glasses were washed with 1× PBS, fixed with 4% PFA for 15 min at RT, and preblocked with 1× PBS++ (containing 10% donkey serum and 0.3% Triton X-100). Next, we incubated the cells with primary antibodies diluted in 1× PBS containing 1% donkey serum, 1% bovine serum albumin (BSA), and 0.1% Triton X-100 for 3 hours at RT, washed the cells with 1× PBS for three times, and stained the cells with secondary antibodies for 2 hours at RT. Last, the stained cells were inversely mounted on glass slides for further imaging.

Single-molecule fluorescence in situ hybridization

Mouse brain sections were prepared as described above, mounted onto SuperFrost Plus microscope slides, and subjected to smFISH using either RNAscope technology or hybridization chain reaction (HCR) approach. For RNAscope assays, the probes targeting against *Kiss1* (#500141-C1) and *Col25a1* (#538511-C2) were designed and validated by Advanced Cell Diagnostics. Briefly, the brain sections were dried at 55°C for 2 hours, rinsed with 1× PBS, treated with 3% hydrogen peroxide in methanol, and subjected to antigen retrieval. Subsequently, the tissue sections were dehydrated with 100% ethanol and incubated with mRNA probes for 2 hours at 40°C. The specific signals were then amplified with multiplexed amplification buffer according to the manufacturer's protocol (Advanced Cell Diagnostics, #323110) and detected with TSA Plus Fluorescence kits (PerkinElmer, #NEL753001KT).

For HCR assays, we used a software to design HCR probes for targeting the mRNA sequence of *Tac2*, *Agrp*, *Pomc*, *Sst*, *Ghrh*, *Adcyap1*, *Pdyn*, and *Gnrh* genes (software available at https://github.com/GradinaruLab/HCRprobe). The sequences of all HCR probes are listed in table S6, and all of them were synthesized by Sangon Biotech, China. Brain sections were permeabilized in 70% ethanol for 16 hours at 4°C, followed by 0.5% Triton X-100 in 1× PBS at 37°C for 1 hour, and treated with protease K (10 μg/ml) to improve mRNA accessibility. After two washes with 1× PBS at RT, sections were prehybridized in 30% probe hybridization buffer for 1 hour at 37°C and then incubated in 30% probe hybridization buffer containing HCR probes (10 mM for each) at 37°C for 3 hours. After mRNA hybridization, the washing and amplification steps were performed as previously described (*26*).

Single-nucleus RNA library preparation and sequencing

The tuberal and mammillary zones of hypothalamus were microdissected from at least three control and three NKO mice at P14 under stereoscope. The tissues were immersed in ice-cold homogenization buffer containing 250 mM sucrose, 25 mM KCl, 5 mM $MgCl_2$, 10 mM tris, 0.1 mM dithiothreitol, mini protease inhibitor cocktail (Roche, #11836153001), ribonuclease inhibitor (0.4 U/μl), 1% BSA, and 0.1% NP-40 and triturated using a glass homogenizer for 10 times. After centrifugation of homogenized tissues at 500*g* for 5 min, we washed the cell pellets with homogenization buffer by repetitive pipetting and separated the nuclei from hypothalamic tissues by centrifuging again. The cell pellets were resuspended with cold 1× PBS to generate single-nucleus suspensions for snRNA-seq. We generated three replicates for both control and NKO groups.

After nucleus counting with hemocytometer, we took advantage of DNBSEQ technology platforms (BGI Genomics, China) and DNBelab C4 Single-Cell Library Prep Set (MGI, #1000021082) for library preparation. Briefly, single-nucleus suspensions were pumped into microfluidic device for droplet generation, followed by emulsion breakage, bead collection, reverse transcription, and cDNA amplification to generate barcoded libraries. The cDNA products were then sheared to short fragments with a length of 250 to 400 bp, and indexed sequencing libraries were constructed according to the manufacturer's protocol. The quality of sequencing libraries was examined by the Qubit ssDNA Assay Kit (Thermo Fisher Scientific, #Q10212). DNBs were loaded into the patterned nano arrays and sequenced on the ultrahigh-throughput DIPSEQ T1 sequencer using the following read length: 30 bp for read 1, inclusive of 10-bp cell barcode 1, 10-bp cell barcode 2, and 10-bp unique molecular identifier (UMI), 100 bp of transcript sequence for read 2, and 10 bp for sample index.

Sequencing data preprocessing

Read preprocessing was performed using 10× Genomics and DNBSEQ workflow. For cells sequenced with 10× Genomics Chromium platform, the Cellranger's pipeline (version 3.0.2) was used for demultiplexing raw sequencing data, barcode assignment, and UMI quantification. Using a prebuilt annotation package, we mapped the reads to the GRCm38 mouse reference genome to generate gene expression matrices. The matrix files arising from different batches of experiments were subsequently integrated and analyzed using Seurat v3 software (*54*). For snRNA-seq data yielded from DNBSEQ platform, the raw sequencing reads were filtered and demultiplexed using PISA (https://github.com/shiquan/PISA). Reads were aligned to GRCm38 mouse genome using STAR (version 2.7.4a) and sorted by Sambamba (version 0.7.0).

Quality control and data integration

For quality control, we selected the cells that satisfied the following criteria for further analysis: (i) There were less than 10% mitochondrial gene counts in collected cells or nuclei; (ii) cells with more than 600 genes or 500 UMIs and nuclei with the number of detected genes between 800 and 8000 met the quality criteria; and (iii) cells and nuclei were not defined as doublet with DoubletFinder (version 2.0.2) (*55*), which averaged the transcriptional profile of randomly chosen cell pairs to create artificial doublets and then predicted the possible doublets according to each cell's proximity in the gene expression space to the artificial doublets. The mean variance normalized bimodality coefficient was calculated to determine the neighborhood size by each sample, and the number of artificial doublets was set to 0.25 as a recommended parameter.

To ensure data accuracy and eliminate the potential bias caused by the integration of data from different platforms, we have combined the data separately for each platform and analyzed them independently with the same workflow. Briefly, the expression matrices from the same platform were combined based on "MergeSeurat" function with Seurat v3 software (*54*).

Dimensionality reduction and clustering

After removing unqualified cells, we normalized the raw reads using the "LogNormalize" subroutine with 10,000 scales, selected the top 2000 variable genes using the "FindVariableFeatures" function, and rescaled the normalized dataset with the "ScaleData" function of Seurat software (*54*). Principal components analysis was performed to reduce the dimensionality of datasets, and the first 50 principal components were inferred using uniform manifold approximation and projection (UMAP) dimensionality reduction. We further performed clustering analysis using a shared nearest neighbor (SNN)–based clustering algorithm, which calculates *K*-nearest neighbors ($K = 20$), constructs an SNN graph, and optimizes the modularity function to determine clusters. For cell clustering, we adopted stepwise clustering strategy for each dataset. First, the cells passing quality control were clustered with the Louvain algorithm in "FindClusters" function at a resolution of 0.5 to distinguish neurons from nonneuronal cells. Subsequently, we subsetted neurons from diverse single-cell datasets for further reclustering. The neuronal clusters were further compared pairwise to identify cell type–specific genes, and

cell identities were assigned by cross-referencing their marker genes with known neuronal subtype markers.

Cell compositional analysis

There were three technical replicates for both WT and NKO groups in our snRNA-seq dataset. To assess the changes in cell composition responding to genetic deletion of *Tbx3* in the hypothalamus, we used three different bioinformatics tools to perform statistical analysis of cell compositional shift: scCODA, Cacoa, and speckle. First, we took advantage of a Bayesian model, named as scCODA software, to conduct single-cell compositional analysis. This model automatically selected an appropriate cell type with least change as the reference and inferred differential abundance of cell types between WT and NKO groups with false discovery rate less than 0.05 (*56*). Second, we used Cacoa approach to analyze the abundance of different cell types and inferred the statistical significance with loading coefficients based on random resampling of replicates and cells across the entire dataset with default parameters. Briefly, we translated the abundance of N neuronal subtypes into N-1 simplex space using isometric log-ratio transformation and then identified loading coefficients within N-1 simplex space to infer compositional shift among NKO cells (*57*). Last, we used speckle (https://github.com/Oshlack/speckle), requiring at least three replicates, to evaluate the difference in cell type proportions in our snRNA-seq data. The Bonferroni multiple comparison test was used to compute the statistical significance between groups, and the cell types with false discovery rate less than 0.05 were identified as neuronal clusters with compositional shift.

Phylogenetic analysis of identity class and transcriptomic similarity analysis

To evaluate the taxonomic relationship between neuronal subtypes in the hypothalamus and the transcriptomic similarity of lost and gained cell subtypes in NKO mice, we used "BuildClusterTree" function in Seurat to construct a phylogenetic tree relating the "average" cell from each identity cluster (*54*). The phylogenetic tree is estimated based on a distance matrix constructed in the gene expression space. The interrelation between neuronal subtypes can only be coarsely represented in hierarchical dendrogram.

To align neuronal subtypes from different single-cell and single-nucleus transcriptomic datasets, we developed an approach to abrogate the batch effect for performing transcriptomic similarity analysis. Briefly, we independently performed normalization, dimensional reduction, neuronal clustering, and signature gene identification for each dataset, selected the top signature genes from each neuronal cluster in different datasets, and calculated the mean expression of these signature genes using "AverageExpression" function as previously described (*58*). After rescaling the simplified data matrix containing the mean expression values of each neuronal subtype, we merged the matrices that would be compared pairwise and then quantified the Pearson correlation coefficients for each cell type pair from two different datasets. The results of transcriptomic similarity analysis were visualized by heatmap and Sankey diagram based on Pheatmap and ggalluvial (http://corybrunson.github.io/ggalluvial/) packages.

Lentivirus package and primary neuronal culture

To package lentivirus encoding Tbx3, we cultured HEK293T cells in DMEM supplemented with 10% FBS, plated 4×10^6 cells on 10-cm dishes at 12 hours before transfection, and transfected the cells with lentiviral construct (pCDH-CMV-Tbx3-EF1-GFP or control plasmids), psPAX2, and pMD2.G at a ratio of 4:3:1 using LipoMax (Sudgen, #32012) according to the manufacturer's instructions. At 48, 72, and 96 hours after transfection, the supernatant with viral particles was collected, pooled, filtered through a 0.45-μm filter (Sartorius, #17598-K), and enriched with a Lenti-X concentrator (Takara, #631232). The viral titer was determined using the Lenti-X qRT-PCR Titration Kit (Takara, #631235), and the lentivirus was aliquoted and stored at −80°C.

Given the nonspecific staining of multiple Tac2 and Kiss1 antibodies in vitro, we determined to use *Tac2-Cre::Ai9* mice to indicate the identity of cultured KNDy neurons. The arcuate nucleus from E16.5 *Tac2-Cre::Ai9* mice was microdissected and treated with digestion solution [papain (10 U/ml; Worthington, #LK003178) and deoxyribonuclease I (100 U/ml; Beyotime, #D7073) in DMEM] at 37°C for 30 min. After digestion, the tissues were dissociated with Pasteur pipettes with finely polished tips, centrifuged at 1000 rpm for 5 min, and resuspended with DMEM to generate single-cell suspension. Next, we plated the cells on the round coverslips coated with poly-D-lysine (10 μg/ml; Sigma-Aldrich, #P1149) and laminin (10 μg/ml; Thermo Fisher Scientific; #23017015) at a density of 6×10^4 cells/cm^2 and left the cells in the incubator for 4 hours. DMEM was then replaced with preheated Neurobasal medium supplemented with 1× B27 (Gibco, #17504044), 1× GlutaMAX (Gibco, #35050061), penicillin (50 U/ml), and streptomycin (5 mg/ml). At 24 hours after plating, we infected the neurons with lentivirus encoding Tbx3 and then maintained the neuronal culture by replacing half of the medium every other day. The cultured neurons were fixed with 4% PFA for quantitative analysis at 10 days in vitro.

Determination of puberty onset and estrous cyclicity

To determine the puberty onset of animals, we monitored the prepubertal littermate mice daily from P22 for preputial separation of males and vaginal opening of females. Exposure of glans penis in male mice and complete canalization of vagina in female mice were regarded as biological signs for puberty onset. We further collected vaginal smears daily after the observation of vaginal opening in female mice and determined the day of their first estrus cycle by identifying cornified cells within vaginal smear.

Estrous cyclicity was monitored by daily vaginal cytology assays for a period of 30 days in 2-month-old female mice. Staging of estrus cycle, divided into proestrus, estrus, metestrus, and diestrus phases, depended on the morphology and proportion of cells observed on a vaginal smear. Proestrus is featured by the dominance of round, nucleated epithelial cells; the appearance of anucleated cornified cells indicates a progression from proestrus to estrus; metestrus phase is characterized by a combination of leukocytes and nucleated and anucleated epithelial cells; and a predominant accumulation of leukocytes occurs within vaginal mucosa during diestrus phase.

Testis histomorphology and ovarian histology

After transcardiac perfusion of animals, testes from males were dissected, weighed, and imaged. Ovaries were dissected from female mice, immersed in 4% PFA overnight at 4°C, dehydrated in 20% sucrose solution for 12 hours, and then embedded in optimal cutting temperature (OCT) compound for hematoxylin and eosin staining. Briefly, ovarian tissue sections were dried for 30 min at RT,

sequentially stained with hematoxylin and eosin solution, dehydrated through an alcohol gradient, and mounted with neutral gum.

Hormonal assays

Animals were anesthetized with intraperitoneal injection of 2,2,2-tribromoethanol, and blood was withdrawn by cardiac puncture (10:00 a.m.). Blood samples were allowed to clot and then centrifuged to collect the resulting supernatant, designated as serum. We measured the basal levels of mouse LH with an enzyme-linked immunosorbent assay (ELISA) kit (AMEKO, #AE90609Mu). Briefly, we added 40 μl of serum samples, 10 μl of anti-LH antibodies, and 50 μl of streptavidin–horseradish peroxidase conjugate into the appropriate wells of assay plates coated with LH antibodies, incubated the plates at 37°C for 1 hour on a plate shaker, and measured the absorbance of the reaction solution with a plate reader (SpectraMAX 190, Molecular Devices, USA). The concentration of LH was determined using the standard curve. The intra-assay and inter-assay coefficients of variance were less than 7%.

Purification of recombinant hTBX3 proteins

To purify recombinant proteins for phase separation assays, we transformed BL21 (DE3) competent cells with plasmids encoding hTBX3 and its pathogenic mutants, allowed the cells to grow at 37°C, and induced protein expression with isopropyl-β-D-thiogalactopyranoside at 16°C for 16 hours. The bacteria were harvested by centrifugation, resuspended, and sonicated. The expressed proteins were incubated with Ni–nitrilotriacetic acid (NTA) resin (GenScript, #L00666), eluted with elution buffer A [150 mM NaCl, 25 mM tris-HCl, 5% glycerol, and 300 mM imidazole (pH 7.5)], loaded onto an MBPTrap HP column (Cytiva, #28918779), and eluted again with elution buffer B (150 mM NaCl, 25 mM tris-HCl, 5% glycerol, and 300 mM imidazole). Next, the collected proteins were incubated with tobacco etch virus protease at 4°C overnight to cleave MBP tags, purified again with Ni-NTA resin to remove the cleaved tags, and eluted with elution buffer C (150 mM NaCl, 25 mM tris-HCl, and 5% glycerol). Last, the purified proteins were concentrated to 200 μM and validated by running SDS–polyacrylamide gel electrophoresis gels.

In vitro phase separation assays

The purified hTBX3 and its mutant proteins were incubated with Alexa Fluor 488/568–C5-maleimide (200 ng/ml; Thermo Fisher Scientific, #A10254 or #A20341) in the dark for 1 hour on the ice. The fluorescence-conjugated proteins were subsequently diluted with dilution buffer containing NaCl with variable concentration (75 to 500 mM), 25 mM tris-HCl (pH 7.5), and 5% glycerol to reach the final concentration of 0.5 to 40 μM. The protein phase separation at different protein and salt concentrations reacted for 30 min at RT, and the images of phase-separated condensates were taken using the Olympus IXplore Spin Spinning Disk Microscope.

Fluorescence recovery after photobleaching

To determine the dynamic fluidity of hTBX3 protein, we prepared the phase-separated droplets of hTBX3 in buffer containing 180 mM NaCl, photobleached the center of droplets with a 488-nm laser pulse (65% intensity), and recorded the fluorescence recovery for 12 min under a Nikon A1 HD25 confocal microscope. The fluorescence baseline was captured 10 s before bleaching. For FRAP data analysis, NIS-Elements AR 5.4 software was used to calibrate the recovery of fluorescence intensity within the bleached droplets.

Cleavage under targets and tagmentation (CUT&Tag) and motif analysis

To conduct CUT&Tag assay, we microdissected the hypothalamus from control and NKO mice, ground the tissues with tissue grinder, and lysed the cells to obtain single-nucleus suspension. We prepared at least 500,000 nuclei for each reaction and followed the bench top CUT&Tag protocol as previously reported (*59*). First, concanavalin A–coated magnetic beads (Bangs Laboratories, #BP531) were incubated with the nuclei for 10 min at RT. Second, the bead-bound nuclei were collected with a magnetic rack and incubated with Tbx3 antibodies (Abcam, ab154828) for 2 hours at 4°C on a rotator, followed by a 1-hour incubation with secondary antibody (Jackson ImmunoResearch Laboratories, #711-165-152). Third, the nuclei on beads were treated with pA-Tn5 transposase for 1 hour at RT on the rotator, which enables the binding of Tn5 to Tbx3 antibodies. Fourth, the tagmentation reaction was triggered by adding specific tagmentation buffer and lasted for 1 hour at 37°C in a thermomixer with shaking at 1000 rpm. Fifth, the tagmentation process was terminated, and the fragmented DNA in supernatant was collected using phenol-chloroform extraction, followed by ethanol precipitation. Sixth, the DNA fragments were processed and amplified with a TruePrep DNA Library Prep kit (Vazyme, #TD501) according to the manufacturer's instructions. Last, the DNA libraries (150 to 500 bp) were collected by AMPure XP beads (Agencourt, #A63882), quantified with DeNovix dsDNA Quantification Assay, and sequenced on the NovaSeq 6000 Sequencing System (Illumina).

Adaptor sequences of all raw reads were removed by Cutadapt, and the sequencing data were mapped to mouse reference genome using Bowtie2 software. After removing duplicate reads with Sambamba software, we used peak calling algorithm MACS2 to identify the potential binding sites of Tbx3 in the mouse genome (*60*) and found two similar binding motifs by analyzing the peak sequences with MEME program (https://meme-suite.org/tools/meme-chip) in our biological replicates. Using the mTbx3 binding motifs obtained from our data and the hTBX3 binding motifs (MA1566.1 and MA1566.2) from JASPAR database (*61*), we predicted the potential binding sites of mTbx3/hTBX3 on the putative promoters (2.1 kb) of *Tac2*/*TAC3* and *Kiss1*/*KISS1* by FIMO (available at https://meme-suite.org/meme/tools/fimo). We set the *P* value less than 0.01 for prediction (table S5).

Luciferase assays

To determine the transcriptional regulation of putative target genes by mTbx3, we seeded HEK293T cells on 24-well plates at a density of 5×10^4 cells/cm^2 and transfected the cells with mTbx3-encoding plasmid, firefly luciferase reporter constructs containing the putative promoters of mouse *Tac2* or *Kiss1* genes, and renilla luciferase. Alternatively, the cells were transfected with expression plasmids encoding hTBX3 or its mutants as well as luciferase reporter constructs containing the promoters of human *TAC3* or *KISS1* to determine the transcriptional regulatory activity of human homologous protein. Luciferase assay was measured at 36 hours after transfection using a Dual Luciferase Reporter Assay kit (Yeasen, #11402ES60). Briefly, the transfected cells were lysed with lysis buffer for 5 min at RT, and the luciferase activity was determined by a microplate reader (BioTek Synergy H1, Agilent Technologies, USA) after adding the substrates.

Statistical analysis

All of the statistical details including the statistical methods, sample numbers, and *P* values can be found in the figures and/or figure

legends. All data collection and data analyses were blinded in this study. All experiments were independently repeated for at least three times. GraphPad Prism, R software, MEGA software, and Microsoft Excel were used for statistical analyses. Group data are presented as mean ± SEM, other than the FRAP quantifications that are presented as mean ± SD. Quantitative values for the neuronal fate induction assay are shown as box plots wherein boxes represent the interquartile range (IQR), whiskers extend to ±1.5 IQR, and bold lines indicate the median values. Two-tailed unpaired Student's *t* test, one-way analysis of variance (ANOVA), two-way ANOVA, and log-rank test were used to quantify the performance. The statistical significance was indicated as follows: $^{*}P < 0.05$; $^{**}P < 0.01$; $^{***}P < 0.001$; $^{\#\#}P < 0.01$; $^{\#\#\#}P < 0.001$; N.S., not significant.

SUPPLEMENTARY MATERIALS

Supplementary material for this article is available at https://science.org/doi/10.1126/sciadv.abq2987

View/request a protocol for this paper from *Bio-protocol*.

REFERENCES AND NOTES

1. V. M. Navarro, Metabolic regulation of kisspeptin—The link between energy balance and reproduction. *Nat. Rev. Endocrinol.* **16**, 407–420 (2020).
2. M. L. Greenwald-Yarnell, C. Marsh, M. B. Allison, C. M. Patterson, C. Kasper, A. MacKenzie, R. Cravo, C. F. Elias, S. M. Moenter, M. G. Myers Jr., ERα in *Tac2* neurons regulates puberty onset in female mice. *Endocrinology* **157**, 1555–1565 (2016).
3. J. C. Gill, V. M. Navarro, C. Kwong, S. D. Noel, C. Martin, S. Xu, D. K. Clifton, R. S. Carroll, R. A. Steiner, U. B. Kaiser, Increased neurokinin B (Tac2) expression in the mouse arcuate nucleus is an early marker of pubertal onset with differential sensitivity to sex steroid-negative feedback than Kiss1. *Endocrinology* **153**, 4883–4893 (2012).
4. V. M. Navarro, F. Ruiz-Pino, M. A. Sanchez-Garrido, D. Garcia-Galiano, S. J. Hobbs, M. Manfredi-Lozano, S. Leon, S. Sangiao-Alvarellos, J. M. Castellano, D. K. Clifton, L. Pinilla, R. A. Steiner, M. Tena-Sempere, Role of neurokinin B in the control of female puberty and its modulation by metabolic status. *J. Neurosci.* **32**, 2388–2397 (2012).
5. S. L. Padilla, J. Qiu, C. C. Nestor, C. Zhang, A. W. Smith, B. B. Whiddon, O. K. Rønnekleiv, M. J. Kelly, R. D. Palmiter, AgRP to Kiss1 neuron signaling links nutritional state and fertility. *Proc. Natl. Acad. Sci. U.S.A.* **114**, 2413–2418 (2017).
6. R. S. Ahima, J. Dushay, S. N. Flier, D. Prabakaran, J. S. Flier, Leptin accelerates the onset of puberty in normal female mice. *J. Clin. Invest.* **99**, 391–395 (1997).
7. S. A. Roberts, U. B. Kaiser, Genetics in Endocrinology: Genetic etiologies of central precocious puberty and the role of imprinted genes. *Eur. J. Endocrinol.* **183**, R107–R117 (2020).
8. S. D. Bianco, U. B. Kaiser, The genetic and molecular basis of idiopathic hypogonadotropic hypogonadism. *Nat. Rev. Endocrinol.* **5**, 569–576 (2009).
9. A. P. Abreu, C. A. Toro, Y. B. Song, V. M. Navarro, M. A. Bosch, A. Eren, J. N. Liang, R. S. Carroll, A. C. Latronico, O. K. Rønnekleiv, C. F. Aylwin, A. Lomniczi, S. Ojeda, U. B. Kaiser, MKRN3 inhibits the reproductive axis through actions in kisspeptin-expressing neurons. *J. Clin. Invest.* **130**, 4486–4500 (2020).
10. A. P. Abreu, A. Dauber, D. B. Macedo, S. D. Noel, V. N. Brito, J. C. Gill, P. Cukier, I. R. Thompson, V. M. Navarro, P. C. Gagliardi, T. Rodrigues, C. Kochi, C. A. Longui, D. Beckers, F. de Zegher, L. R. Montenegro, B. B. Mendonca, R. S. Carroll, J. N. Hirschhorn, A. C. Latronico, U. B. Kaiser, Central precocious puberty caused by mutations in the imprinted gene MKRN3. *N. Engl. J. Med.* **368**, 2467–2475 (2013).
11. M. G. Teles, S. D. C. Bianco, V. N. Brito, E. B. Trarbach, W. Kuohung, S. Xu, S. B. Seminara, B. B. Mendonca, U. B. Kaiser, A. C. Latronico, A GPR54-activating mutation in a patient with central precocious puberty. *N. Engl. J. Med.* **358**, 709–715 (2008).
12. L. G. Silveira, S. D. Noel, A. P. Silveira-Neto, A. P. Abreu, V. N. Brito, M. G. Santos, S. D. C. Bianco, W. Kuohung, S. Xu, M. Gryngarten, M. E. Escobar, I. J. P. Arnhold, B. B. Mendonca, U. B. Kaiser, A. C. Latronico, Mutations of the KISS1 gene in disorders of puberty. *J. Clin. Endocrinol. Metab.* **95**, 2276–2280 (2010).
13. E. D. Louden, A. Poch, H. G. Kim, A. Ben-Mahmoud, S. H. Kim, L. C. Layman, Genetics of hypogonadotropic hypogonadism-human and mouse genes, inheritance, oligogenicity, and genetic counseling. *Mol. Cell. Endocrinol.* **534**, 111334 (2021).
14. E. Galazzi, P. Duminuco, M. Moro, F. Guizzardi, N. Marazzi, A. Sartorio, S. Avignone, M. Bonomi, L. Persani, M. T. Bonati, Hypogonadotropic hypogonadism and pituitary hypoplasia as recurrent features in ulnar-mammary syndrome. *Endocr. Connect.* **7**, 1432–1441 (2018).
15. N. Bertrand, D. S. Castro, F. Guillemot, Proneural genes and the specification of neural cell types. *Nat. Rev. Neurosci.* **3**, 517–530 (2002).
16. E. S. Deneris, O. Hobert, Maintenance of postmitotic neuronal cell identity. *Nat. Neurosci.* **17**, 899–907 (2014).
17. A. J. Washkowitz, S. Gavrilov, S. Begum, V. E. Papaioannou, Diverse functional networks of Tbx3 in development and disease. *Wiley Interdiscip. Rev. Syst. Biol. Med.* **4**, 273–283 (2012).
18. S. F. Khan, V. Damerell, R. Omar, M. du Toit, M. Khan, H. M. Maranyane, M. Mlaza, J. Bleloch, C. Bellis, B. D. B. Sahm, J. Peres, K. N. ArulJothi, S. Prince, The roles and regulation of TBX3 in development and disease. *Gene* **726**, 144223 (2020).
19. M. Bamshad, R. C. Lin, D. J. Law, W. S. Watkins, P. A. Krakowiak, M. E. Moore, P. Franceschini, R. Lala, L. B. Holmes, T. C. Gebuhr, B. G. Bruneau, A. Schinzel, J. G. Seidman, C. E. Seidman, L. B. Jorde, Mutations in human TBX3 alter limb, apocrine and genital development in ulnar-mammary syndrome. *Nat. Genet.* **16**, 311–315 (1997).
20. M. Bamshad, T. le, W. S. Watkins, M. E. Dixon, B. E. Kramer, A. D. Roeder, J. C. Carey, S. Root, A. Schinzel, L. van Maldergem, R. J. M. Gardner, R. C. Lin, C. E. Seidman, J. G. Seidman, R. Wallerstein, E. Moran, R. Sutphen, C. E. Campbell, L. B. Jorde, The spectrum of mutations in TBX3: Genotype/phenotype relationship in ulnar-mammary syndrome. *Am. J. Hum. Genet.* **64**, 1550–1562 (1999).
21. C. Quarta, A. Fisette, Y. Xu, G. Colldén, B. Legutko, Y. T. Tseng, A. Reim, M. Wierer, M. C. de Rosa, V. Klaus, R. Rausch, V. V. Thaker, E. Graf, T. M. Strom, A. L. Poher, T. Gruber, O. le Thuc, A. Cebrian-Serrano, D. Kabra, L. Bellocchio, S. C. Woods, G. O. Pflugfelder, R. Nogueiras, L. Zeltser, I. C. Grunwald Kadow, A. Moon, C. García-Cáceres, M. Mann, M. Treier, C. A. Doege, M. H. Tschöp, Functional identity of hypothalamic melanocortin neurons depends on Tbx3. *Nat. Metab.* **1**, 222–235 (2019).
22. M. Pontecorvi, C. R. Goding, W. D. Richardson, N. Kessaris, Expression of Tbx2 and Tbx3 in the developing hypothalamic-pituitary axis. *Gene Expr. Patterns* **8**, 411–417 (2008).
23. K. S. Eriksson, E. Mignot, T-box 3 is expressed in the adult mouse hypothalamus and medulla. *Brain Res.* **1302**, 233–239 (2009).
24. J. L. Ferran, L. Puelles, J. L. R. Rubenstein, Molecular codes defining rostrocaudal domains in the embryonic mouse hypothalamus. *Front. Neuroanat.* **9**, 46 (2015).
25. L. Puelles, J. L. R. Rubenstein, A new scenario of hypothalamic organization: Rationale of new hypotheses introduced in the updated prosomeric model. *Front. Neuroanat.* **9**, 27 (2015).
26. Y. H. Zhang, M. Xu, X. Shi, X.-L. Sun, W. Mu, H. Wu, J. Wang, S. Li, P. Su, L. Gong, M. He, M. Yao, Q.-F. Wu, Cascade diversification directs generation of neuronal diversity in the hypothalamus. *Cell Stem Cell* **28**, 1483–1499.e8 (2021).
27. R. A. Romanov, E. O. Tretiakov, M. E. Kastriti, M. Zupancic, M. Häring, S. Korchynska, K. Popadin, M. Benevento, P. Rebernik, F. Lallemend, K. Nishimori, F. Clotman, W. D. Andrews, J. G. Parnavelas, M. Farlik, C. Bock, I. Adameyko, T. Hökfelt, E. Keimpema, T. Harkany, Molecular design of hypothalamus development. *Nature* **582**, 246–252 (2020).
28. D. Nicetto, K. S. Zaret, Role of H3K9me3 heterochromatin in cell identity establishment and maintenance. *Curr. Opin. Genet. Dev.* **55**, 1–10 (2019).
29. D. Vasiliauskas, R. Johnston, C. Desplan, Maintaining a stochastic neuronal cell fate decision. *Genes Dev.* **23**, 385–390 (2009).
30. S. Lukassen, E. Bosch, A. B. Ekici, A. Winterpacht, Single-cell RNA sequencing of adult mouse testes. *Sci. Data* **5**, 180192 (2018).
31. X. Long, Q. Yang, J. Qian, H. Yao, R. Yan, X. Cheng, Q. Zhang, C. Gu, F. Gao, H. Wang, L. Zhang, F. Guo, Obesity modulates cell-cell interactions during ovarian folliculogenesis. *iScience* **25**, 103627 (2022).
32. K. Wagh, D. A. Garcia, A. Upadhyaya, Phase separation in transcription factor dynamics and chromatin organization. *Curr. Opin. Struct. Biol.* **71**, 148–155 (2021).
33. A. Boija, I. A. Klein, B. R. Sabari, A. Dall'Agnese, E. L. Coffey, A. V. Zamudio, C. H. Li, K. Shrinivas, J. C. Manteiga, N. M. Hannett, B. J. Abraham, L. K. Afeyan, Y. E. Guo, J. K. Rimel, C. B. Fant, J. Schuijers, T. I. Lee, D. J. Taatjes, R. A. Young, Transcription factors activate genes through the phase-separation capacity of their activation domains. *Cell* **175**, 1842–1855.e16 (2018).
34. D. Hnisz, K. Shrinivas, R. A. Young, A. K. Chakraborty, P. A. Sharp, A phase separation model for transcriptional control. *Cell* **169**, 13–23 (2017).
35. G. A. Tanteles, N. Nicolaou, A. Syrimis, R. Metaxa, M. Nicolaou, V. Christophidou-Anastasiadou, N. Skordis, Novel TBX3 mutation in a family of Cypriot ancestry with ulnar-mammary syndrome. *Clin. Dysmorphol.* **26**, 61–65 (2017).
36. J. Ladewig, P. Koch, O. Brustle, Leveling Waddington: The emergence of direct programming and the loss of cell fate hierarchies. *Nat. Rev. Mol. Cell Biol.* **14**, 225–236 (2013).
37. W. Zhong, Diversifying neural cells through order of birth and asymmetry of division. *Neuron* **37**, 11–14 (2003).
38. D. Jukam, C. Desplan, Binary fate decisions in differentiating neurons. *Curr. Opin. Neurobiol.* **20**, 6–13 (2010).
39. O. Hobert, Terminal selectors of neuronal identity. *Curr. Top. Dev. Biol.* **116**, 455–475 (2016).
40. C. F. Kao, H. H. Yu, Y. He, J. C. Kao, T. Lee, Hierarchical deployment of factors regulating temporal fate in a diverse neuronal lineage of the *Drosophila* central brain. *Neuron* **73**, 677–684 (2012).

41. D. P. Orquera, S. Nasif, M. J. Low, M. Rubinstein, F. S. J. de Souza, Essential function of the transcription factor Rax in the early patterning of the mammalian hypothalamus. *Dev. Biol.* **416**, 212–224 (2016).
42. A. Stoykova, D. Treichel, M. Hallonet, P. Gruss, Pax6 modulates the dorsoventral patterning of the mammalian telencephalon. *J. Neurosci.* **20**, 8042–8050 (2000).
43. S. Han, S. Okawa, G. A. Wilkinson, H. Ghazale, L. Adnani, R. Dixit, L. Tavares, I. Faisal, M. J. Brooks, V. Cortay, D. Zinyk, A. Sivitilli, S. Li, F. Malik, Y. Ilnytskyy, V. E. Angarica, J. Gao, V. Chinchalongporn, A.-M. Oproescu, L. Vasan, Y. Touahri, L. A. David, E. Raharjo, J.-W. Kim, W. Wu, W. Rahmani, J. A.-W. Chan, I. Kovalchuk, L. Attisano, D. Kurrasch, C. Dehay, A. Swaroop, D. S. Castro, J. Biernaskie, A. D. Sol, C. Schuurmans, Proneural genes define ground-state rules to regulate neurogenic patterning and cortical folding. *Neuron* **109**, 2847–2863.e11 (2021).
44. S. Lodato, B. J. Molyneaux, E. Zuccaro, L. A. Goff, H. H. Chen, W. Yuan, A. Meleski, E. Takahashi, S. Mahony, J. L. Rinn, D. K. Gifford, P. Arlotta, Gene co-regulation by Fezf2 selects neurotransmitter identity and connectivity of corticospinal neurons. *Nat. Neurosci.* **17**, 1046–1054 (2014).
45. S. León, C. Fergani, R. Talbi, C. A. Maguire, A. Gerutshang, S. B. Seminara, V. M. Navarro, Tachykinin signaling is required for induction of the preovulatory luteinizing hormone surge and normal luteinizing hormone pulses. *Neuroendocrinology* **111**, 542–554 (2021).
46. R. Lapatto, J. C. Pallais, D. Zhang, Y.-M. Chan, A. Mahan, F. Cerrato, W. W. Le, G. E. Hoffman, S. B. Seminara, Kiss1$^{-/-}$ mice exhibit more variable hypogonadism than Gpr54$^{-/-}$ mice. *Endocrinology* **148**, 4927–4936 (2007).
47. C. Mayer, U. Boehm, Female reproductive maturation in the absence of kisspeptin/GPR54 signaling. *Nat. Neurosci.* **14**, 704–710 (2011).
48. N. Nandankar, A. L. Negrón, A. Wolfe, J. E. Levine, S. Radovick, Deficiency of arcuate nucleus kisspeptin results in postpubertal central hypogonadism. *Am. J. Physiol. Endocrinol. Metab.* **321**, E264–E280 (2021).
49. S. Leon, R. Talbi, E. A. McCarthy, K. Ferrari, C. Fergani, L. Naule, J. H. Choi, R. S. Carroll, U. B. Kaiser, C. F. Aylwin, A. Lomniczi, V. M. Navarro, Sex-specific pubertal and metabolic regulation of Kiss1 neurons via Nhlh2. *eLife* **10**, e69765 (2021).
50. J. Loyal, D. R. Laub, Ulnar-mammary syndrome: Clinical presentation, genetic underpinnings, diagnosis, and treatment. *Eplasty* **14**, ic35 (2014).
51. U. Emechebe, P. Kumar P, J. M. Rozenberg, B. Moore, A. Firment, T. Mirshahi, A. M. Moon, T-box3 is a ciliary protein and regulates stability of the Gli3 transcription factor to control digit number. *eLife* **5**, e07897 (2016).
52. M. P. Colasanto, S. Eyal, P. Mohassel, M. Bamshad, C. G. Bonnemann, E. Zelzer, A. M. Moon, G. Kardon, Development of a subset of forelimb muscles and their attachment sites requires the ulnar-mammary syndrome gene Tbx3. *Dis. Model. Mech.* **9**, 1257–1269 (2016).
53. L. A. Jerome-Majewska, G. P. Jenkins, E. Ernstoff, F. Zindy, C. J. Sherr, V. E. Papaioannou, Tbx3, the ulnar-mammary syndrome gene, and Tbx2 interact in mammary gland development through a p19Arf/p53-independent pathway. *Dev. Dyn.* **234**, 922–933 (2005).
54. T. Stuart, A. Butler, P. Hoffman, C. Hafemeister, E. Papalexi, W. M. Mauck III, Y. Hao, M. Stoeckius, P. Smibert, R. Satija, Comprehensive integration of single-cell data. *Cell* **177**, 1888–1902.e21 (2019).
55. C. S. McGinnis, L. M. Murrow, Z. J. Gartner, DoubletFinder: Doublet detection in single-cell RNA sequencing data using artificial nearest neighbors. *Cell Syst.* **8**, 329–337 (2019).
56. M. Buttner, J. Ostner, C. L. Muller, F. J. Theis, B. Schubert, scCODA is a Bayesian model for compositional single-cell data analysis. *Nat. Commun.* **12**, 6876 (2021).
57. V. Petukhov, A. Igolkina, R. Rydbirk, S. Mei, L. Christoffersen, K. Khodosevich, P. V. Kharchenko, Case-control analysis of single-cell RNA-seq studies. bioRxiv 2022.03.15.484475 [Preprint]. 18 March 2022.https://doi.org/10.1101/2022.03.15.484475.
58. J. M. Kebschull, E. B. Richman, N. Ringach, D. Friedmann, E. Albarran, S. S. Kolluru, R. C. Jones, W. E. Allen, Y. Wang, S. W. Cho, H. Zhou, J. B. Ding, H. Y. Chang, K. Deisseroth, S. R. Quake, L. Luo, Cerebellar nuclei evolved by repeatedly duplicating a conserved cell-type set. *Science* **370**, eabd5059 (2020).
59. H. S. Kaya-Okur, S. J. Wu, C. A. Codomo, E. S. Pledger, T. D. Bryson, J. G. Henikoff, K. Ahmad, S. Henikoff, CUT&Tag for efficient epigenomic profiling of small samples and single cells. *Nat. Commun.* **10**, 1930 (2019).
60. Y. Zhang, T. Liu, C. A. Meyer, J. Eeckhoute, D. S. Johnson, B. E. Bernstein, C. Nusbaum, R. M. Myers, M. Brown, W. Li, X. S. Liu, Model-based analysis of ChIP-seq (MACS). *Genome Biol.* **9**, R137 (2008).
61. O. Fornes, J. A. Castro-Mondragon, A. Khan, R. van der Lee, X. Zhang, P. A. Richmond, B. P. Modi, S. Correard, M. Gheorghe, D. Baranašić, W. Santana-Garcia, G. Tan, J. Chèneby, B. Ballester, F. Parcy, A. Sandelin, B. Lenhard, W. W. Wasserman, A. Mathelier, JASPAR 2020: Update of the open-access database of transcription factor binding profiles. *Nucleic Acids Res.* **48**, D87–D92 (2020).

Acknowledgments: We thank Y. Nakagawa for intensive discussion and X. Xu for comments on the manuscript. We acknowledge Z. Yang, X. Xu, H. Zeng, and J. Han for providing diverse mouse strains for genetic labeling and manipulation. **Funding:** This study was supported by the National Key R&D Program of China (2019YFA0801900 and 2018YFA0801104), the National Natural Science Foundation of China (81891002, 32070972, 31921002, and 31771131), the Strategic Priority Research Program of Chinese Academy of Sciences (XDB32020000), the Hundred-Talent Program (Chinese Academy of Sciences), and the Beijing Municipal Science and Technology Commission (Z210010 and Z181100001518001). **Author contributions:** Q.-F.W. conceived and supervised the project. Q.-F.W., J.K., and D.P. constructed the *Tbx3-CreER^{T2}* mouse strain. X.S., M.X., L.G., X.-L.S., and Q.-F.W. collected brain samples and performed lineage tracing, immunohistochemistry, immunocytochemistry, in situ hybridization, and imaging. Z.C., W.L., M.X., C.L., and L.L. conducted scRNA-seq, snRNA-seq, and bioinformatics analyses. Y.Z., X.S., X.-L.S., and Y.L. purified proteins and performed phase separation and luciferase assays. X.S., X.K., and Y.Z. prepared plasmids, packaged lentivirus, and performed cell culture. X.S., H.Z., and D.J. performed CUT&Tag assay and identified binding motifs. Q.-F.W., Y.L., X.S., and S.Z.H.W. developed the theory and wrote the manuscript. **Competing interests:** The authors declare that they have no competing interests. **Data and materials availability:** All animals and unique/stable reagents generated in this study are available from the corresponding authors with a completed materials transfer agreement. All sequencing data reported in this study are available from the Gene Expression Omnibus through the accession number GEO: GSE195472. The code for bioinformatics analysis is available at https://zenodo.org/record/7131719 for the sake of reproducibility. All other data needed to evaluate the conclusions in the paper are present in the paper and/or the Supplementary Materials.

Submitted 28 April 2022
Accepted 23 September 2022
Published 16 November 2022
10.1126/sciadv.abq2987